Highlights

On the quieting of glaciohydraulic tremor

Małgorzata Chmiel, Nicoletta Caldera, Florent Gimbert, Gerrit Olivier, Alberto Guadagnini, Dominik Gräff, Manuela Köpfli, Mauro A. Werder, Fabian Walter

- Interferometry and matched-field processing characterize glaciohydraulic tremor source (GHT)
- Coherent GHT sources persist while their seismic power drops
- GHT quieting reaches ∼2 dB at 10–20 Hz and repeats during rising water pressure
- Near-complete conduit filling of broad conduits can raise friction, cut discharge ∼28% and quiet GHT
- Local filling redistributes water and pressure across the subglacial drainage system

On the quieting of glaciohydraulic tremor

Małgorzata Chmiel[a,b], Nicoletta Caldera[b,c,d], Florent Gimbert[e], Gerrit Olivier[f], Alberto Guadagnini[c], Dominik Gräff[g], Manuela Köpfli[g], Mauro A. Werder[d], Fabian Walter[b]

[a] *CNRS, Observatoire de la Côte d'Azur, Université Côte d'Azur, IRD, Géoazur, 250 rue Albert Einstein, Sophia Antipolis, 06560, Valbonne, France*
[b] *Swiss Federal Institute for Forest, Snow and Landscape Research WSL, Zürcherstrasse 111, Birmensdorf, 8903, Switzerland*
[c] *Department of Civil and Environmental Engineering, Politecnico di Milano, Piazza Leonardo Da Vinci 32, Milano, 20133, Italy*
[d] *ETH Zurich, Laboratory of Hydraulics, Hydrology and Glaciology (VAW), Hönggerbergring 26, Zürich, 8093, Switzerland*
[e] *UGA - IGE CNRS, 460 rue de la Piscine 38400, Saint-Martin-d'Hères, 38400, France*
[f] *University of Tasmania, Churchill Ave, Hobart, 7005, Australia*
[g] *Department of Earth and Space Sciences, University of Washington, 3920 Okanogan Lane NE, Seattle, 98195, Washington, United States*

Abstract

The subglacial hydraulic system strongly modulates glacier motion, yet the links between subglacial water flow, basal pressure, and short-lived drainage reorganization remain difficult to observe directly. Seismology can track seismic power generated by turbulent subglacial water flow, known as glaciohydraulic tremor (GHT). At Rhône Glacier, Switzerland, previous observations documented periods of GHT quieting around stick-slip tremor during elevated basal water pressure, but the physical origin of this quieting remained incompletely understood. Here, we combine seismic power analysis, matched-field processing, borehole water-pressure measurements, surface velocity, runoff, and hydraulic-potential routing to investigate the origin of GHT quieting. The quieting is strongest in the 10–20 Hz band and recurs across stick-slip episodes, whereas the 6–8 Hz band shows a weaker response. Matched-field processing shows that coherent GHT sources persist during quieting near an inferred subglacial drainage pathway, suggesting reduced hydraulic–seismic coupling rather than disappearance of the hydraulic source. Physics-based hydraulic calculations show that near-complete filling of broad, low-aspect-ratio conduits can increase wetted perimeter and frictional resistance, producing modeled local discharge reductions of ∼20–28% and seismic-power decreases of ∼1.2–1.8 dB. We interpret GHT quieting as a seismic signature of transient drainage reorganization during rising basal water pressure. Our results suggest that localized, transiently flow-limiting drainage elements can redistribute water across the wider subglacial drainage system, modulating basal water pressure and glacier motion well beyond the element itself. More broadly, cryoseismic observations can help identify short-lived changes in drainage-system state, hydraulic resistance, and ice–water coupling beneath glaciers.

Keywords: Cryoseismology, Glacier Hydraulics, Glaciohydraulic tremor, Matched Field Processing (MFP), Seismic interferometry

---

1. Introduction

Subglacial hydrology plays an important role in regulating glacier motion across a wide range of temporal and spatial scales (Iken and Bindschadler, 1986; Schoof, 2010; Flowers, 2015). Variations in basal water pressure can reduce the effective pressure (i.e., the difference between ice-overburden and basal water pressure, also referred to as effective stress) at the bed, alter ice–bed coupling, and promote rapid accelerations and stick-slip motion

(Fowler, 1987; Lipovsky and Dunham, 2017).

On temperate glaciers, where liquid water coexists with glacier ice, surface meltwater and precipitation reach the glacier bed through open crevasses and moulins (Cuffey and Paterson, 2010). Once at the bed, water may follow a range of drainage configurations, including thin films (Weertman, 1972), permeable sediments (Boulton, 1972; Clarke, 1987), linked cavities (Walder, 1986), and channelized systems such as ice-walled R-channels (Hooke et al., 1990; Nye, 1965; Röthlisberger, 1972; Walder and Fowler, 1994). Seasonal drainage evolution typically involves a transition from inefficient distributed drainage toward more efficient channelized flow as melt supply increases (Lliboutry, 1968; Röthlisberger, 1972). Yet, how conduit-scale geometry and transient increases in basal water pressure reorganize drainage structure and modify ice–water interactions at the bed remains incompletely understood.

Addressing this question is challenging because the glacier bed is difficult to access, and subglacial observations are sparse. Borehole measurements provide local time series of basal water pressure (e.g., Andrews et al., 2014; Iken et al., 1976), active seismic experiments can image basal structure at a given point in time (e.g., Nolan and Echelmeyer, 1999), similar to ground-penetrating radar characterizing englacial and subglacial material properties (e.g., Stuart et al., 2003), and dye tracer experiments yield insights into the lumped effect of water pathways through and beneath glaciers (e.g., Werder et al., 2009). However, these approaches generally provide spatially sparse or temporally limited snapshots, making it difficult to resolve short-timescale reorganization of drainage processes at conduit scale.

Multiple studies have shown that continuous seismic monitoring offers a complementary approach (Podolskiy and Walter, 2016) and can provide new insights into fundamental englacial and subglacial processes, such as frictional glacier basal motion (e.g., Gräff and Walter, 2021; Helmstetter et al., 2015; Lipovsky et al., 2019; Lipovsky and Dunham, 2017), formation and propagation of cracks and crevasses (e.g., Chmiel et al., 2023; Faillettaz et al., 2011; Mikesell et al., 2012), and subglacial water flow (e.g., Gimbert et al., 2016; Nanni et al., 2021, 2020; Lindner et al., 2020). Similar to river-induced seismic noise (Burtin et al., 2008; Gimbert et al., 2014), subglacial water flow generates seismic tremors (Bartholomaus et al., 2015). These tremors, referred to as "glaciohydraulic tremor" (GHT), arise both due to pressure variations acting on the bed and walls of subglacial channels during turbulent flow (Gimbert et al., 2016) and particle-ground impacts during bedload transport (Tsai et al., 2012). The amplitude, frequency content, and spatial organization of these signals can provide indicators of ongoing hydraulic processes (Bartholomaus et al., 2015; Gimbert et al., 2016; Nanni et al., 2020; Köpfli et al., 2022). Seismic array methods, such as Matched Field Processing (Kuperman and Turek, 1997), can locate coherent tremor sources and track changes in their spatial distribution, providing constraints on the organization and evolution of subglacial drainage (Nanni et al., 2022, 2021).

Recently, Köpfli et al. (2022) documented repeated periods of GHT quieting immediately before and after stick-slip tremors at Rhône Glacier (German: *Rhonegletscher*), Switzerland. This quieting was expressed as a decrease of a few decibels in seismic power, most clearly in the 10–20 Hz band, during intervals of rising basal water pressure. Köpfli et al. (2022) hypothesized that the quieting reflects transient changes in subglacial drainage conditions, potentially linked to hydraulic limitations within the drainage system. However, identifying the physical mechanisms underlying this quieting requires a more detailed characterization of GHT source generation and its relationship to evolving subglacial drainage conditions.

Here, we build on these initial findings by combining multi-day seismic and glaciological observations with seismic interferometry, matched-field processing, and physics-based hydraulic modeling to characterize the source, spatial organization, and possible physical origin of GHT quieting. We analyze two frequency bands, 10–20 Hz and 6–8 Hz, to test whether GHT quieting and source location vary with frequency. We show that GHT systematically weakens prior to stick-slip tremor, with stronger suppression in the 10–20 Hz band, and that coherent sources persist during quieting near the inferred subglacial drainage pathway. The MFP locations in the 10–20 Hz band are more spatially concentrated than the 6–8 Hz band. We interpret these observations using a roof-friction framework in which near-complete conduit filling modifies wetted perimeter, frictional resistance, and the efficiency of turbulent seismic radiation. By linking frequency-dependent tremor quieting and source localization to conduit-scale hydraulic processes, we provide new constraints on short-lived subglacial drainage reorganization during rising basal water pressure.

2. Study site and data

2.1. Rhône glacier and field setting

The Rhône Glacier is an 8-km-long and up to 350 m thick Alpine glacier located in the Swiss Alps (Fig. 1A). It flows southward from 3,600 to 2,200 m above sea level (ASL) with an average surface slope of 10° and a glacier area of ∼15.2 km^2 (Bauder et al., 2020). Our study site was located in the ablation zone of the glacier (elevation of ∼2500 m ASL and a local surface slope of ∼7°), where the glacier was about 200 m thick in 2020 (Gräff and Walter, 2021) and the glacier ice is at the pressure melting point (Rutishauser et al., 2016).

2.2. Data

Data used in this study were collected during the 2020 melt season. Seismic instrumentation consisted of two arrays: a near-surface seismic array (aperture 521 m) and a smaller borehole seismic array englacially deployed ∼40 m above the glacier bed (aperture 60 m). The near-surface array operated between July 2 and August 26, 2020 and consisted of eight 3-component borehole seismometers (Lennartz 3D/BHs, natural frequency 1 Hz, sampling frequency: 500 Hz) and installed in shallow boreholes at depths of 5 m. The borehole array operated between July 22 and August 20, 2020 and consisted of five borehole geophones (ASIR AG4.5, natural frequency: 4.5 Hz, sampling frequency: 2,000 Hz) installed at depths of ∼150 m below the ice surface within boreholes drilled with the hot water method (Iken et al., 1976).

Additional measurements accompanied the seismic instrumentation. Ice-surface motion at the drilling site was monitored using Global Navigation

Satellite System (GNSS) receivers, with positions sampled every 15 s and processed kinematically. Measured positions were quality-controlled by removing epochs with large standard deviations and resampled values showing excessive scatter or unphysical position changes (e.g., associated with antenna adjustments). The filtered time series was smoothed with a 6-h rolling mean and resampled to hourly intervals. Three-dimensional surface velocities V_{3D} (in $\mathrm{cm\,d^{-1}}$) were derived from successive position differences, with positional uncertainties propagated to the velocity estimates (Gräff, 2021).

Subglacial water pressure was measured at the glacier bed using six piezoresistive pressure sensors installed at the bottom of boreholes drilled through ~180 m of ice. The records were acquired at 2 kHz on a data logger and resampled to 1-min intervals; no further processing was applied. Several sensors suffered from electronic problems during acquisition. We use only the record from the most reliable sensor, which limits the coverage of the pressure observations (Fig. 1C).

Proglacial discharge was measured at Gletsch by the Swiss Federal Office for the Environment. Because the gauging station at Gletsch lies downstream of the proglacial lake and ~3 km from the glacier terminus, the measured runoff is delayed relative to discharge at the glacier terminus by transient storage in the proglacial lake (Ogier, 2024) and additional routing between the lake and the gauge.

The locations of instruments and previously mapped stick-slip tremor sources by Köpfli et al. (2022) are shown in Fig. 1. Figure 2 illustrates a representative glacio-hydraulic tremor quieting preceding stick-slip tremor event, as first documented by Köpfli et al. (2022).

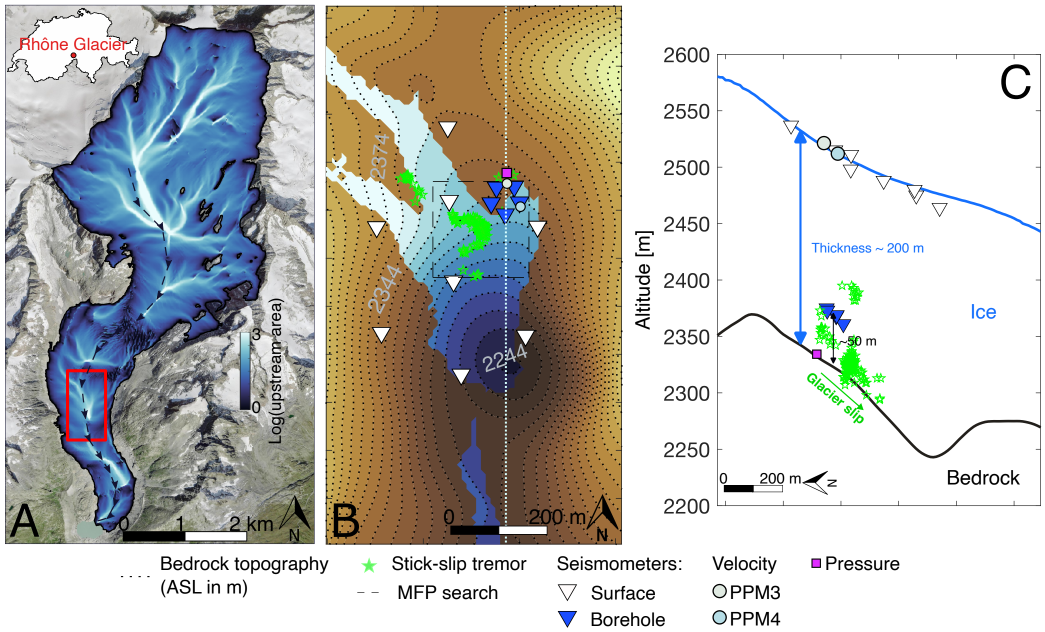

Figure 1: Study setting at Rhône Glacier, Switzerland. (A) Orthoimage of Rhône Glacier (2021; source: Swiss Federal Office of Topography). Blue shading shows $\log_{10}$ upstream area, highlighting possible subglacial drainage pathways, the red box marks the study area shown in (B). The inset map indicates the glacier location in Switzerland. (B) Zoom on the study area. Blue shading highlights the upper 20% of $\log_{10}$ upstream-area values ($\geq$80th percentile) within the panel B domain, interpreted as a proxy for likely subglacial drainage pathways, the remaining area is shown in brown. Dotted lines show bedrock-elevation contours (m ASL) from interpolated ground-penetrating radar surveys (Grab et al., 2021), darker shading indicates lower bed elevation. White inverted triangles denote near-surface seismometers and blue inverted triangles denote deep-borehole geophones. Circles indicate GNSS stations (PPM3, PPM4) and the magenta square marks the borehole pressure sensor. Green stars show stick-slip event clusters from Köpfli et al. (2022). The black dashed square delineates the Matched-Field Processing (MFP) search domain used for source localization. The white line indicates the cross-section shown in (C). (C) Cross-section through the array showing the ice surface (blue) and bedrock (black) from Grab et al. (2021), together with instrument geometries, and stick-slip tremor locations. Ice thickness was ~200 m in the study area.

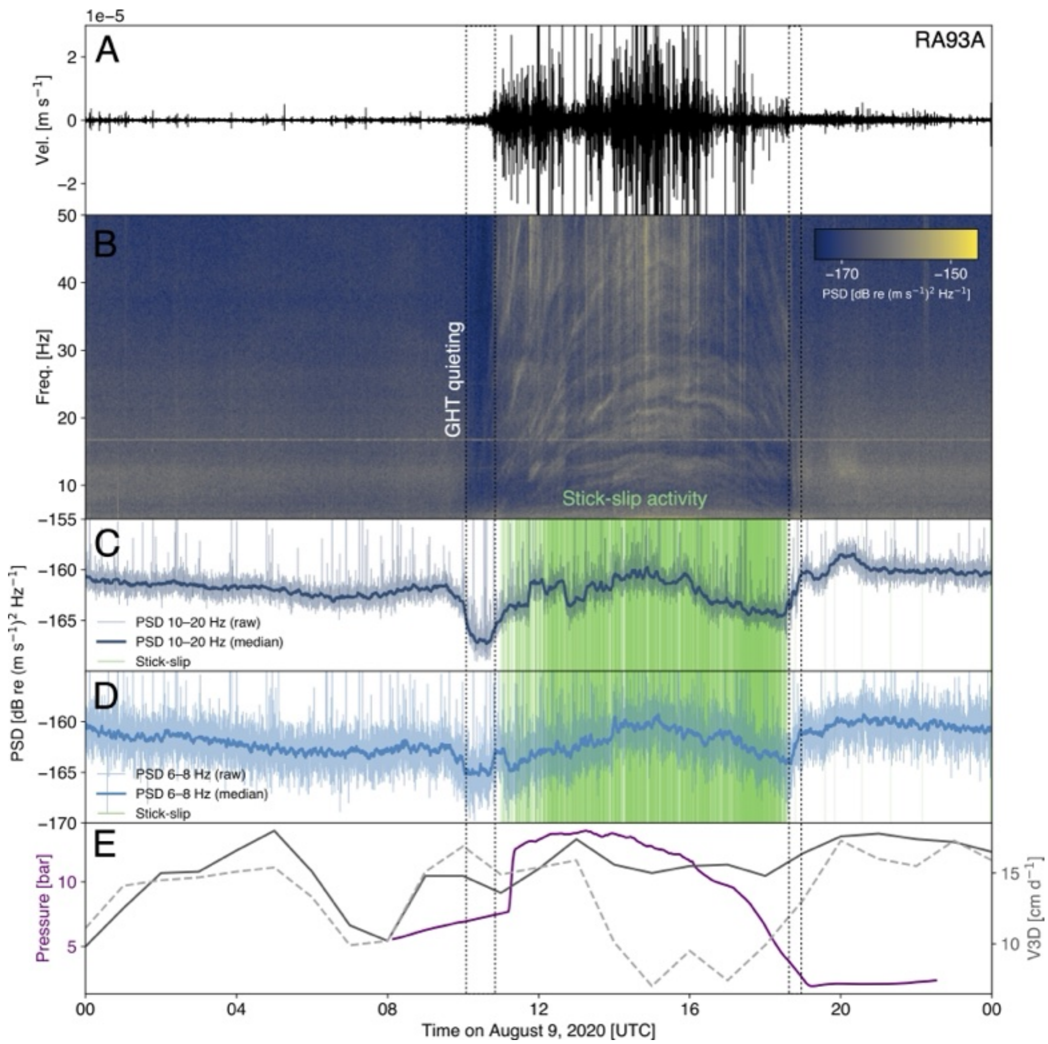

Figure 2: Example of daily measurements illustrating the relationship between glaciohydraulic tremor (GHT) quieting, stick-slip activity, and borehole water pressure at Rhône Glacier (9 August 2020). Black dashed lines mark the GHT quieting intervals occurring before and after the stick-slip activity. (A) Vertical-component ground velocity showing the onset of stick-slip activity tremor. (B) Spectrogram illustrating temporal variations in seismic power (power spectral density, PSD, in dB re 1 $(\mathrm{m\,s^{-1}})^2\,\mathrm{Hz^{-1}}$). The horizontal line at $\sim$16.7 Hz corresponds to the 16 2/3-Hz power supply of the Swiss railway system, generated by nearby hydropower turbines, and is unrelated to glacial processes. (C) PSD in the 10–20 Hz and (D) in the 6–8 Hz range (thin line: raw, thick line: 5-min running-median). Vertical green lines mark stick-slip event times from Köpfli et al. (2022). (E) Borehole water pressure (purple, left axis) and GNSS surface speed V_{3D} at stations PPM3 (solid gray) and PPM4 (dashed gray, right axis; $\mathrm{cm\,d^{-1}}$).

3. Methods

3.1. Shreve routing

Our study period (mid-July to August) corresponds to the late melt season, when subglacial drainage systems commonly contain both distributed and channelized components as meltwater input increases (Röthlisberger, 1972; Fountain and Walder, 1998; Schoof, 2010; Flowers, 2015; Werder et al., 2013). We use Shreve routing to obtain a first-order estimate of hydraulically favorable drainage pathways beneath the study area. Subglacial water flow is commonly approximated as following gradients in hydraulic potential, defined as the sum of water-pressure potential and elevation potential (Shreve, 1972):

$$\phi = \rho_w g z_b + K \rho_i g h_i \tag{1}$$

where ρ_w and ρ_i are the densities of water and ice, g is gravitational acceleration, z_b is bed elevation, h_i is ice thickness, and $K = p_w/p_i$ is the flotation fraction representing the ratio of basal water pressure to ice overburden pressure. We adopt $K = 0.8$, consistent with in situ basal pressure measurements reaching up to $p_w = 14$ bar (Köpfli et al., 2022) and an ice thickness of approximately 200 m in the study area. Likely drainage pathways were identified by computing the upstream contributing area, defined as the cumulative area of hydraulically connected grid cells flowing along hydraulic-potential gradients (Flowers, 2015). Upstream area was computed with a multiple-flow-direction algorithm (Freeman, 1991), in which each cell distributes its accumulated area among all lower-potential neighbors in proportion to the potential gradient toward each neighbor.

We note that Shreve-type routing with $K > 0$ assumes pressurized drainage conditions, with $K = 1$ representing the full-flotation end member and $K = 0$ purely topography-controlled routing. It can therefore provide a first-order estimate of hydraulically favorable drainage pathways, even though real drainage elements may operate at sub-overburden pressure or locally transition between partially filled and pressurized states. We interpret the routing results as indicators of likely drainage organization rather than instantaneous hydraulic states.

The blue area shown in the Fig. 1B and the blue contours shown in Fig. 5 indicate the inferred drainage-pathway outline derived from the Shreve-routing result, defined by thresholding the upstream-area grid to retain cells with upstream-area values above the 80th percentile of the $K = 0.8$ routing result. Because the flotation factor K is expected to vary spatially and temporally in real drainage systems, we tested the sensitivity of the inferred routing pattern to the assumed pressure fraction by repeating the hydraulic-potential routing for $K = 0, 0.7, 0.8, 0.9$, and 1.0, where $K = 0$ corresponds to purely topography-controlled routing and $K = 1$ to full flotation. The location of the main inferred pathway beneath the seismic array persists across this full range, although its geometry and secondary branches vary (Fig. E.1). The $K = 0.8$ case is used as the reference routing in the main figures.

3.2. Multi-day average analysis of seismic power, water pressure, velocity, and runoff

To investigate the quieting of GHT, we analyze the daily evolution of seismic power, basal water pressure, surface velocity, and runoff, stacked as medians across the eight stick-slip tremor days for which pressure data are available (5–9, 11, 13, and 19 August 2020). GHT quieting is observed both immediately before and after stick-slip tremor episodes (Fig. 2, Köpfli et al., 2022). We restrict quantitative analysis to the pre-stick-slip phase, since GHT cannot be separated from stick-slip tremor during active slip and the variable duration of stick-slip episodes prevents consistent alignment of the post-stick-slip quieting across events.

We analyze seismic power in two frequency bands, 10–20 Hz and 6–8 Hz. The 10–20 Hz band is where GHT quieting is most pronounced at Rhône Glacier (Köpfli et al., 2022). The 6–8 Hz band provides a lower-frequency reference within the range in which glaciohydraulic tremor has been identified at other glaciers (e.g., Bartholomaus et al., 2015; Gimbert et al., 2016), including source imaging of subglacial water flow at Argentière Glacier in the 3–7 Hz band (Nanni et al., 2021, 2020). The lower bound of 6 Hz is set by the response of the borehole geophones (natural frequency 4.5 Hz), below which the instrument response might limit reliable power estimates. Comparing the two bands allows us to test whether the quieting and the spatial organization of GHT sources are frequency dependent.

Daily time series were aligned relative to the onset of the pre-stick-slip seismic power decrease in the 10–20 Hz band to account for variability in event timing. The onset of the pre–stick-slip quieting in the 10–20 Hz band was manually identified for each event based on the initial drop of seismic power preceding stick-slip tremor. Seismic power spectral density (PSD) was computed for each borehole station using 10 s sliding windows with 50% overlap and estimated via Welch's method from vertical-component velocity records. Band-averaged power in the 10–20 Hz and 6–8 Hz was expressed in dB relative to 1 $(\mathrm{m\,s^{-1}})^2\,\mathrm{Hz^{-1}}$, averaged across stations using the median, and smoothed with a 15 min moving mean filter. Seismic power spectral density (PSD) was normalized per event by subtracting the median baseline value prior to stacking to remove inter-event PSD amplitude offsets. Basal water pressure, surface velocity, and runoff were analyzed in absolute units.

All time series were resampled to a common 1-minute time vector prior to analysis. For each variable, the median across days is computed and variability is shown as the interquartile range. GNSS-derived surface velocity was averaged across the two stations to obtain a representative three-dimensional surface velocity.

3.3. Seismic interferometry

Seismic interferometry (e.g., Nakata et al., 2019) allows imaging and monitoring of subsurface processes by retrieving empirical Green's functions from continuous ambient seismic vibrations. We apply this approach to investigate the stability and seismic characteristics of the glaciohydraulic tremor source. Ambient noise cross-correlations were computed for the vertical components of the borehole stations over a 30-day period (22 July–20 August 2020). Correlations were calculated using 5-minute time windows with a maximum lag of 8 s in the 6–200 Hz frequency band (Fig. 3A). All computations were performed using the MSNoise framework (Lecocq et al., 2014). The resulting noise correlations were analyzed to evaluate temporal changes in apparent velocity and seismic phase stability associated with the GHT source.

3.4. Matched-Field Processing

Matched-field processing (MFP) is an array-based technique (Kuperman and Turek, 1997) that estimates source location by maximizing phase coherence between observed and modeled wavefield across a seismic network. We apply a Bartlett MFP using a homogeneous velocity model (that is optimized based on the MFP output value, which ranges from 0 to 1). Higher MFP output indicates a better match between the recorded wavefield and the model. We applied MFP to continuous seismic wavefields to locate persistent coherent ambient-noise sources associated with GHT, rather than to locate discrete impulsive sources such as stick-slip tremor or crevassing events. For each 5 min time window, we kept the optimized MFP source location and its associated MFP output.

We combined five borehole stations with three nearby surface stations to improve spatial resolution in the region of observed stick-slip tremor activity. An initial unconstrained MFP applied to a 3D grid search (10 m spacing in x, y, and z) located tremor sources at elevations corresponding to the glacier bed (Figs. 4B and E.2). Guided by this result, we performed a full analysis within a vertically constrained search space centered on the known bed topography, while keeping a horizontal search region defined by the array aperture to improve horizontal location accuracy. Because vertical resolution is limited by the array geometry, we do not interpret small vertical variations in source position. Robustness tests using the full array and an expanded search volume produce similar horizontal source-density patterns and indicate source locations at the glacier bed (Fig. E.3). For the full month of data, MFP was combined with a Nelder–Mead optimization scheme (Lagarias et al., 1998;

Nelder and Mead, 1965; Chmiel et al., 2019) and applied to both borehole and surface stations in two frequency bands (6–8 Hz and 10–20 Hz).

To compare the spatial organization of glaciohydraulic tremor across different stages of the stick-slip cycle, MFP localizations were grouped into three time periods: non-stick-slip periods, pre-stick-slip quieting, and stick-slip. Post-stick-slip quieting intervals, identified manually from the 10–20 Hz PSD in the same way as the pre-stick-slip quieting, were excluded from the non-stick-slip category, so that the non-stick-slip maps represent baseline conditions outside the quieting–stick-slip sequence. Prior to mapping, we excluded sources located on the horizontal boundaries of the search grid, sources converging on the upper vertical boundary, and localizations with MFP output lower than the random-coherence level 1/N, where N is the number of stations. The remaining 3D locations were projected onto the horizontal plane and binned into a regular $5\,\mathrm{m} \times 5\,\mathrm{m}$ grid. For each grid cell, MFP outputs were summed and then normalized by the total summed MFP output within each period and frequency band. This representation highlights regions where MFP localizations are both frequent and associated with high MFP output and normalization removes differences in the total number of detections between periods. Further methodological details are provided in Appendix B and in Chmiel et al. (2016, 2019); Nanni et al. (2020).

3.5. Physical seismic model

Turbulent water flow within subglacial conduits generates fluctuating wall-pressure and shear stresses that radiate seismic energy (Gimbert et al., 2016). The resulting seismic waves propagate through the glacier and can be recorded by nearby sensors. We adopt the mechanistic framework of

Gimbert et al. (2016), originally developed for rivers (Gimbert et al., 2014) and extended to subglacial channels. In this model, turbulent wall-pressure fluctuations are assumed to be approximately uniform along the conduit boundary, and the coupling between hydraulic forcing and seismic radiation is parameterized through conduit geometry and flow conditions.

Following Gimbert et al. (2016), seismic power generated by turbulent conduit flow can be expressed in scaling form as:

$$P_w \propto \beta^{-1/4} S^{41/24} Q^{5/4}, \tag{2}$$

or equivalently,

$$P_w \propto \beta^{-11/3} R^{-82/9} Q^{14/3}, \tag{3}$$

where Q is discharge, S is hydraulic pressure gradient, R is hydraulic radius, and β parameterizes conduit geometry and degree of filling.

These two expressions highlight different end-member dependencies: for approximately constant pressure gradient, seismic power scales mainly as $Q^{5/4}$, whereas for fixed conduit geometry (β and R constant) it scales more strongly with discharge as $Q^{14/3}$.

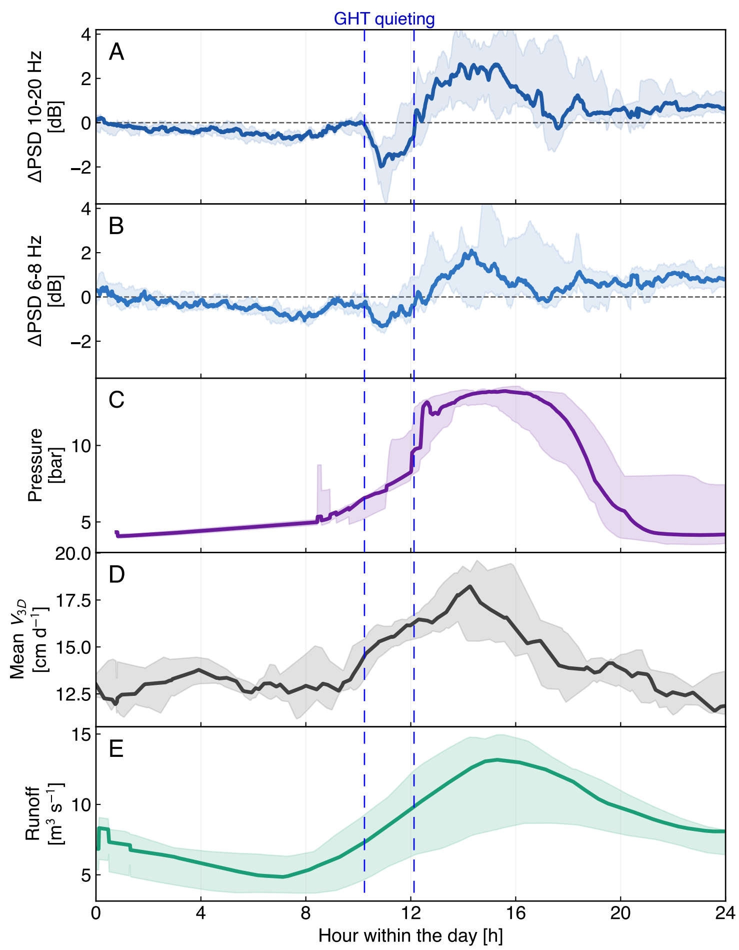

Figure 3: Multi-day median evolution of seismic power, basal water pressure, surface velocity, and runoff aligned to the onset of pre–stick-slip GHT quieting. (A) Median power spectral density (PSD) in the 10–20 Hz band. (B) Median PSD in the 6–8 Hz band. (C) Basal water pressure. (D) Mean three-dimensional surface velocity derived from GNSS observations. (E) Proglacial runoff. All time series are aligned relative to the onset of the daily pre–stick-slip decrease in 10–20 Hz seismic power. Solid lines show the median across eight stick-slip days for which pressure data are available, shaded envelopes indicate the interquartile range. The 10–20 Hz band exhibits a pronounced transient decrease in seismic power preceding peak pressure and velocity, whereas the 6–8 Hz band shows a weaker response.

4. Results

4.1. GHT quieting preceding stick-slip tremor

A representative stick-slip tremor episode on 9 August 2020 illustrates the characteristic sequence of seismic and hydrological changes (Fig. 2). Before the onset of stick-slip tremor, seismic power in the 10–20 Hz band drops by 5 dB and persists for approximately one hour before stick-slip onset. In contrast, the 6–8 Hz band shows a weaker decrease (~2 dB, Fig. 2B–C). The onset of GHT quieting precedes the main stick-slip phase and coincides with a rise in basal water pressure (Fig. 2E). Pressure reaches peak values of 14 bar shortly after stick-slip initiation. For this single event, surface velocity does not show a clear response.

To assess the repeatability of this sequence, we aligned eight stick-slip days to the onset of the 10–20 Hz quieting and computed the median evolution across events (Fig. 3). In the aligned median curves, 10–20 Hz seismic power first decreases by nearly 2 dB and then recovers during a period of elevated basal water pressure, which plateaus at almost 14 bar, corresponding to ~80% of the local ice overburden pressure for ~200 m of ice. The pressure record itself documents rapid transitions in the basal hydraulic state, varying diurnally from near-atmospheric values to this plateau, so that the bed switches between unpressurized and nearly fully pressurized conditions on timescales of hours. GHT quieting systematically occurs on the rising limb of these pressurization cycles (Figs. 2 and 3).

The 6–8 Hz band shows a weaker decrease of ~ 1 dB. Surface velocity reaches its maximum during the high-pressure plateau, whereas proglacial runoff follows a broader daily cycle and peaks after the pressure increase

(Fig. 3E). The multi-day curves are aligned to the quieting onset rather than to stick-slip times to characterize the recurring hydromechanical evolution associated with GHT quieting. A decrease of 2 dB corresponds to a ∼37% reduction in seismic power, and a 1 dB decrease corresponds to ∼21% reduction. The full time series for August 5-13 (the period with the most stick-slip tremors) are shown in Fig. E.4.

4.2. Seismic source characterization of glaciohydraulic tremor through seismic interferometry

Noise cross-correlations between borehole stations RA91A-RA93A show persistent coherent arrivals throughout the monitoring period, interrupted during stick-slip tremor episodes (Fig. 4A). The strongest coherence occurs in the acausal branch of the correlations, indicating that coherent energy propagates predominantly from the direction of station RA93A toward RA91A rather than isotropically: for a spatially uniform noise field, both correlation branches would carry similar energy, whereas the observed one-sided dominance requires a persistent source located on one side of the station pair (e.g., Stehly et al., 2006). This asymmetry is maintained throughout the monitoring period, indicating that the source position is stable in time. The coherent energy is concentrated below 50 Hz, with dominant energy at 10–20 Hz (spectrogram of the acausal branch in Fig. E.5), coinciding with the frequency band in which GHT quieting is strongest (Köpfli et al., 2022).

The dominant arrivals on the vertical–vertical correlations correspond to apparent velocities of $V_{s,\mathrm{app}} \sim 2130\,\mathrm{m\,s^{-1}}$ and $V_{p,\mathrm{app}} \sim 4260\,\mathrm{m\,s^{-1}}$, estimated from the correlation arrival times and the RA91A–RA93A interstation distance (Fig. 4A). These values are higher than typical body-wave velocities in temperate glacier ice (Podolskiy and Walter, 2016; Walter et al., 2020). If the dominant GHT source is offset from the interstation axis, the retrieved arrivals do not propagate exactly along the station pair, and the resulting apparent velocities overestimate the true medium velocities.

The asymmetry of the correlations indicates that the dominant source is located preferentially toward station RA93A, southwest of the borehole array. Weaker causal arrivals at higher frequencies are also observed and likely reflect scattered body-wave energy (e.g., Wapenaar, 2006). Additional frequency-dependent correlation examples are provided in Fig. E.6. In summary, the interferometric analysis indicates a persistent, directionally stable source of coherent seismic energy located toward the southwest of the borehole array, radiating predominantly below 50 Hz with dominant energy at 10–20 Hz, and sampled by the borehole pair through body-wave arrivals.

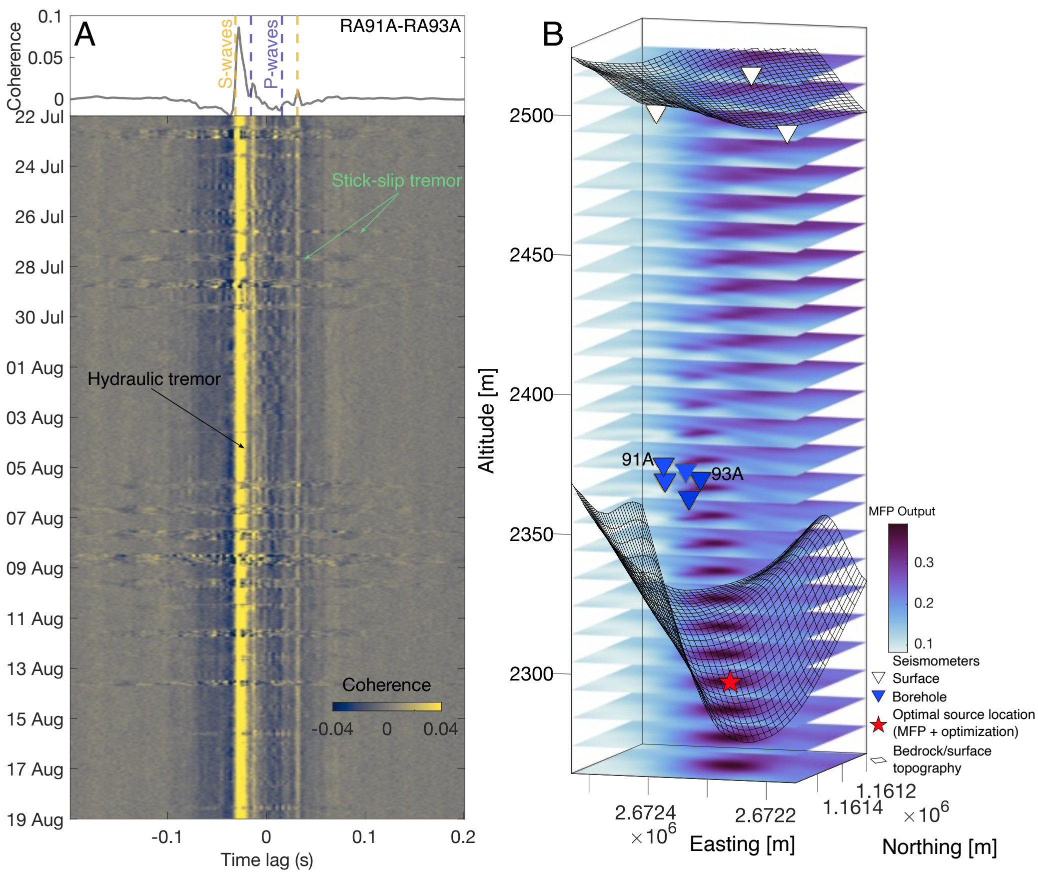

Figure 4: Characterization of glaciohydraulic tremor using seismic interferometry and matched-field processing. (A) Noise cross-correlations between borehole stations RA91A and RA93A computed over the 1-month monitoring period in the 6–200 Hz frequency band. The lower panel shows daily correlation functions, and the upper panel shows the mean correlation stack. Dashed lines indicate theoretical direct P- and S-wave arrivals based on Walter et al. (2020). (B) Example three-dimensional source localization obtained with matched-field processing using three surface and five borehole stations for a 5 min time window on 9 August 2020 at 00:00 UTC. The red star marks the optimized source location obtained using MFP combined with Nelder–Mead optimization. The black mesh indicate the radar-derived glacier bed and surface (Grab et al., 2021).

4.3. Spatial distribution of glaciohydraulic tremor sources

Shreve routing identifies a main hydraulically favorable pathway beneath the instrumented area, with an inferred drainage junction located close to the borehole array (Fig. 1B). Routing sensitivity tests show that the location of the main inferred drainage pathway remains stable from $K = 0$ (topography-controlled routing) to $K = 1.0$ (full flotation), indicating that the pathway position is set primarily by bed topography and is robust to the assumed hydraulic state, although local upstream-area values and secondary pathways vary (Fig. E.1).

Matched-field processing (MFP) applied to the combined borehole and surface array enables three-dimensional localization of GHT sources. Fig. 4B shows an example source location obtained from a 5 min window in the 10–20 Hz band using three surface and five borehole stations. Overall, the MFP localizations indicate a dominant source region beneath the borehole array (Figs. E.2 and E.3). Although the combined array improves source-depth sensitivity compared to a surface-only geometry, vertical resolution remains limited. We therefore focus the following analysis on horizontal source distributions.

In the 10–20 Hz band, MFP localizations define a compact source region with approximate dimensions of 35 m × 40 m (Fig. 5A–C). This region lies close to the inferred drainage junction and to previously reported stick-slip tremor locations (Köpfli et al., 2022). In contrast, the 6–8 Hz band produces a broader and less compact source distribution. We also observe less coherent source localization in the downglacier part of the array.

MFP-density maps show frequency-dependent differences in the spatial distribution of coherent seismic energy between non-stick-slip, pre-stick-slip quieting, and stick-slip periods (Fig. 5). In the 10–20 Hz band, MFP localizations remain concentrated near the central drainage area during all periods (Fig. 5A–C). Coherent MFP localizations remain present during quieting, indicating that GHT energy persists despite the reduction in seismic power. During stick-slip, two localized maxima are observed along the inferred drainage pathway (Fig. 5C). The 6–8 Hz band shows a broader, elongated distribution during non-stick-slip periods and remains more distributed along the inferred drainage pathway during quieting and stick-slip (Fig. 5D–F). Overall, the 10–20 Hz band remains concentrated near the central drainage area between non-stick-slip, quieting, and stick-slip periods, whereas the 6–8 Hz band shows more variable localizations along the inferred drainage pathway.

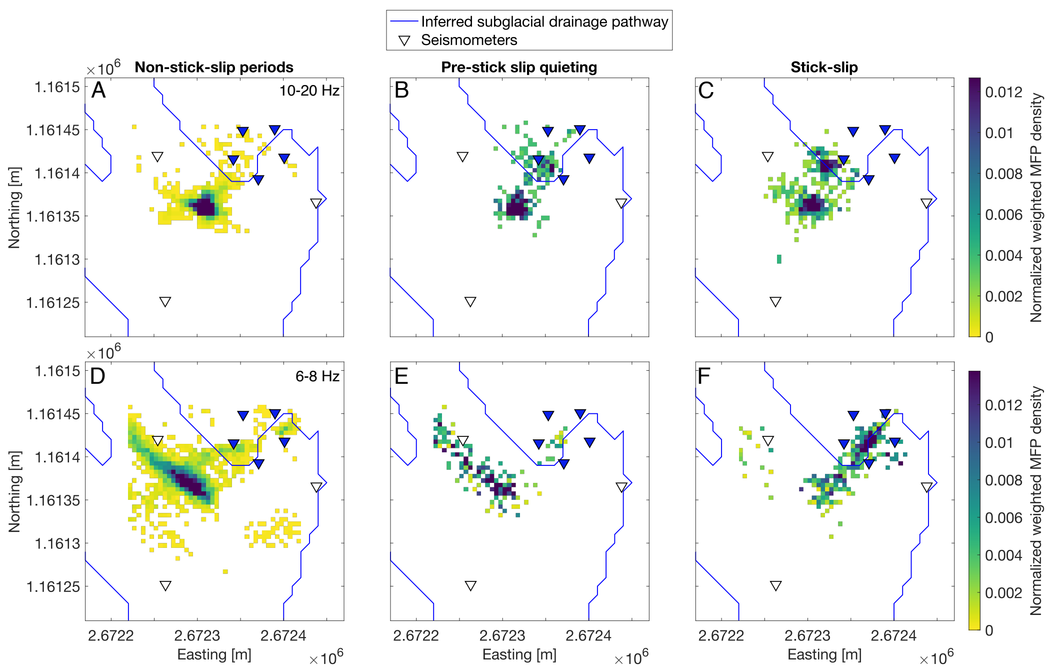

Figure 5: Spatial distribution of glaciohydraulic tremor localizations during different stick-slip periods. Normalized weighted MFP-density maps for the 10–20 Hz band (A–C) and 6–8 Hz band (D–F) during non-stick-slip periods, pre-stick-slip quieting, and stick-slip. Each map shows the horizontal projection of quality-controlled MFP source locations (source depths are not represented), binned onto a 5 m × 5 m horizontal grid, with cell values given by the summed MFP output normalized by the total summed MFP output for that phase and frequency band. Blue lines indicate the inferred subglacial drainage pathway from Shreve routing, and inverted triangles mark seismic stations. The 10–20 Hz tremor becomes more spatially focused during pre-stick-slip quieting, whereas the 6–8 Hz tremor remains distributed along the inferred drainage pathway.

5. Discussion

5.1. GHT quieting reflects reduced seismic radiation, not disappearance of the hydraulic source

Seismic power in the 1–20 Hz frequency range has previously been interpreted as a seismic expression of turbulent subglacial water flow at Rhône Glacier (e.g., Canassy et al., 2016; Clyne et al., 2023; Köpfli et al., 2022) and other glaciers (e.g., Gimbert et al., 2016; Nanni et al., 2021; Bartholomaus et al., 2015; Lindner et al., 2020). We therefore interpret the coherent source analyzed here as GHT based on the combined evidence that it occurs within this frequency range, persists outside discrete stick-slip and crevassing events, and localizes near the radar-derived bed and inferred subglacial drainage pathway in the MFP analysis (Nanni et al., 2022, 2021).

Our observations show that GHT weakens prior to the high-water-pressure period associated with stick-slip tremor (Köpfli et al., 2022), but does not disappear. Seismic power decreases most strongly in the 10–20 Hz band, whereas the 6–8 Hz band shows a weaker reduction. At the same time, coherent MFP localizations remain present during the pre-stick-slip quieting period and continue to cluster near the inferred subglacial drainage pathway. We therefore interpret quieting as a reduction in seismic radiation from an active hydraulic source, rather than disappearance of the hydraulic source itself.

5.2. Frequency-dependent quieting indicates scale-dependent hydraulic processes

The decrease in seismic power is stronger in the 10–20 Hz band than in the 6–8 Hz band, suggesting that the two bands are sensitive to different spatial or hydraulic scales within the drainage system. The 10–20 Hz MFP density is more spatially concentrated and localizes near the inferred drainage junction, whereas the 6–8 Hz band remains more broadly distributed along the drainage pathway (Fig. 5). Part of this difference might reflect a lower spatial resolution at longer wavelengths. However, the 6–8 Hz density is not an isotropically broadened version of the high-frequency distribution. It is organized along the inferred drainage pathways, extending over both routing branches, and responds differently in time, consistent with a contribution from larger-scale, spatially distributed water flow.

The less well-defined MFP density in the downglacier part of the array may reflect lower turbulent seismic radiation efficiency, reduced localization sensitivity, or spatially variable drainage connectivity in that region. Localized high-shear or turbulent flow conditions near the inferred drainage junction could enhance high-frequency tremor generation. Because the seismic power of turbulent water flow depends on channel geometry, hydraulic radius, pressure gradient, and discharge (Gimbert et al., 2016; Nanni et al., 2020; Bartholomaus et al., 2015), variations in the high-frequency component of GHT may reflect localized, transient changes in the filling state and wetted perimeter of the drainage pathway. In addition, sediment transport may contribute to the high-frequency tremor (Tsai et al., 2012; Gimbert et al., 2014), because bedload flux scales strongly with flow velocity, a reduction in local flow speed during conduit pressurization would disproportionately suppress this contribution, although our data do not allow us to separate the two source processes.

In contrast, the weaker reduction in 6–8 Hz power is consistent with continued subglacial flow during quieting, potentially associated with larger-scale channelized flow, similar to subglacial water flow source locations imaged on Argentière Glacier in the 3–7 Hz frequency band (Nanni et al., 2021). The broader 6–8 Hz MFP distribution also follows the two inferred drainage branches visible in the upstream-area routing, consistent with a more spatially distributed component of the drainage system.

5.3. A roof-friction mechanism for GHT quieting

The decrease in GHT power during rising basal water pressure may be explained by a transient reduction in turbulent channel flow or in the efficiency of seismic radiation from that flow. In the framework of Gimbert et al. (2016), seismic power depends on discharge, hydraulic pressure gradient, hydraulic radius, and conduit geometry. A rapid increase in basal water pressure could therefore reduce GHT power if it decreases the local hydraulic pressure gradient, reduces flow velocity, or modifies the conduit geometry controlling hydraulic resistance (Schoof, 2010; Werder et al., 2013).

A good candidate mechanism is the transition from partially filled to pressurized conduit flow. As water level rises and contacts the conduit roof, the wetted perimeter increases, which can increase frictional resistance and reduce the amplitude of the generated seismic noise for a given hydraulic gradient (Chow et al., 1988; Schuler and Fischer, 2009). Free-surface conduit flow can occur under glaciers where the bed slope-driven potential gradient is large (Hewitt et al., 2012; Hooke, 1984), with a local channel slope of $\sim 12^\circ$, our study area falls in this regime, and transient increases in water supply can then drive local transitions from free-surface to pressurized flow.

Direct support for episodically non-pressurized drainage conditions at our site comes also from the borehole pressure record, which drops to near-atmospheric values (a minimum of 0.78 bar, see Fig. E.4 and Köpfli et al., 2022). Because borehole camera observations indicate that the borehole did not intersect an active subglacial stream (Gräff, 2021), these drops show that bed regions adjacent to the inferred drainage pathway are at times not pressurized, making open-channel (partially filled) flow in the nearby conduit likely during these intervals.

To quantify this effect, we consider two idealized conduit geometries illustrated in Fig. 6. The first is a semi-circular R-channel of radius $r = 2\,\mathrm{m}$ (Röthlisberger, 1972). The second is a broad, low-aspect-ratio conduit for which small changes in water level near complete filling can strongly modify the wetted perimeter (geometries shown in Fig. 6A and B, respectively). Such geometries are possible for subglacial drainage elements (Flowers, 2015). Ground-penetrating radar observations at Rhône Glacier reveal broad conduits with widths of $17 \pm 1.7\,\mathrm{m}$ and heights of order $0.4\,\mathrm{m}$ (Church et al., 2021), and we adopt these observed dimensions directly as the conduit width w and height d in our calculations (Table 1). The two geometries have comparable cross-sectional areas ($\sim$6.3 and $\sim$6.8 m^2, respectively), so that differences in their modeled response reflect conduit shape rather than conduit size. To capture a range of roof geometries, we consider a deep roof ($d_{\mathrm{roof}} = 0.1\,d$) and a shallow roof ($d_{\mathrm{roof}} = 0.01\,d$), chosen to bracket the roof curvature (not resolved by the radar observations) between a moderately vaulted and a nearly flat roof. The perfectly flat roof ($d_{\mathrm{roof}} \to 0$) provides the analytic end member evaluated below.

We use the approach of Schuler and Fischer (2009) to express the subglacial channel discharge based on the Darcy–Weisbach formulation (Chow et al., 1988):

$$Q = \left(\frac{8g}{f} \frac{\partial H}{\partial x} \frac{A_w^3}{\Gamma_w} \right)^{1/2}, \tag{4}$$

where Q is channel discharge, $H = h + z$ is hydraulic head, $h = p_w/(\rho_w g)$ is pressure head, z is bed elevation, p_w is water pressure, ρ_w is water density, g is gravitational acceleration, f is the dimensionless Darcy–Weisbach friction factor, A_w is the water-filled cross-sectional area, and Γ_w is the wetted perimeter.

Equation 4 shows that discharge increases with the water-filled cross-sectional area A_w, but decreases with increasing wetted perimeter Γ_w, which represents greater frictional resistance along the conduit walls. To isolate the effect of changing wetted perimeter during near-complete filling, we approximate the hydraulic head gradient by the channel slope, $\partial H/\partial x \approx \tan\theta$, where θ is the channel slope.

For each geometry, we calculate the water-filled cross-sectional area A_w, wetted perimeter Γ_w, hydraulic radius, and discharge as a function of filling depth y. We then estimate the associated seismic-power change using the conservative scaling $P_w \propto Q^{5/4}$ from Gimbert et al. (2016), which relates discharge variations to seismic-power variations under an approximately constant hydraulic pressure gradient. This assumption is consistent with our model setup, in which the head gradient is fixed at the channel slope to isolate the effect of the changing wetted perimeter. The alternative fixed-geometry end member ($P_w \propto Q^{14/3}$) assumes a constant hydraulic radius, which does not apply during filling, and would yield several-fold larger modeled power changes. Our estimates are therefore conservative.

Fig. 6C–F shows that the discharge–filling relationship becomes non-unique as the conduit approaches complete filling. At high filling levels, the relative increase in wetted perimeter increases more rapidly than relative increase in water-filled area, so that the ratio A_w^3/Γ_w in Eq. (4), and hence the local channel discharge, decreases even as the water input into the subglacial drainage system further increases, the excess input being transiently stored and redistributed within the drainage system. This effect marks the transition from partially filled to pressurized flow, as water surface initially contacts the conduit roof.

The magnitude of the modeled discharge and seismic-power reduction depends strongly on conduit geometry. Near-complete filling of the semi-circular R-channel produces only a small discharge reduction of 4.5%, corresponding to a seismic-power decrease of $< 0.5\,\mathrm{dB}$. The deep-roof geometry produces a larger discharge reduction of 20%, corresponding to an $\sim$1.1 dB decrease in seismic power, while the very shallow-roof geometry produces a discharge reduction of 27% and a $\sim$1.7 dB seismic power decrease. These values are comparable to the observed GHT quieting, suggesting that increased frictional resistance during roof contact can indeed contribute to the reduction in seismic power.

The rooftop geometry is an idealized end-member representation of a

Physical constant	Value	Unit
Gravitational acceleration g	9.8	m s^{-2}
Parameter		
Channel slope θ	12	°
Friction factor f	0.5	–
Channel radius r	2	m
Channel width w	17	m
Channel height d	0.4	m
Roof height d_{roof}	$10\%d$, $1\%d$	m

Table 1: Physical constants and parameter values used in the Schuler and Fischer (2009) model. Conduit width w and height d are taken from ground-penetrating radar observations at Rhône Glacier (Church et al., 2021), the R-channel radius r is chosen to give a comparable cross-sectional area.

broad, low-aspect-ratio conduit. In the case of a perfectly flat roof ($d_{\text{roof}} \to 0$, i.e., a rectangular conduit), the transition to complete filling produces a discontinuity in both Q and modeled seismic power, which can be evaluated analytically: at roof contact, the wetted perimeter jumps from $w+2d$ to $2(w+d)$ at constant cross-sectional area, so that $Q_{\text{full}}/Q_{\text{free}} = [(w+2d)/(2(w+d))]^{1/2}$. For the observed conduit dimensions ($w = 17\,\text{m}$, $d = 0.4\,\text{m}$; Church et al., 2021), this yields an instantaneous local discharge reduction of $\sim$28% and a seismic-power decrease of $\sim$1.8 dB.

Thus, near-complete conduit filling can increase wetted perimeter and frictional resistance, temporarily reducing discharge and flow velocity and decreasing turbulent seismic radiation, while the flow itself remains turbulent. The framework of Schuler and Fischer (2009) provides a simple physical mechanism by which this transition can produce GHT quieting. This mechanism is proposed as a working hypothesis: it is consistent with the observed amplitude and timing of the quieting, but confirming it would require additional constraints, such as direct observations of conduit filling state or co-located pressure measurements along a drainage element.

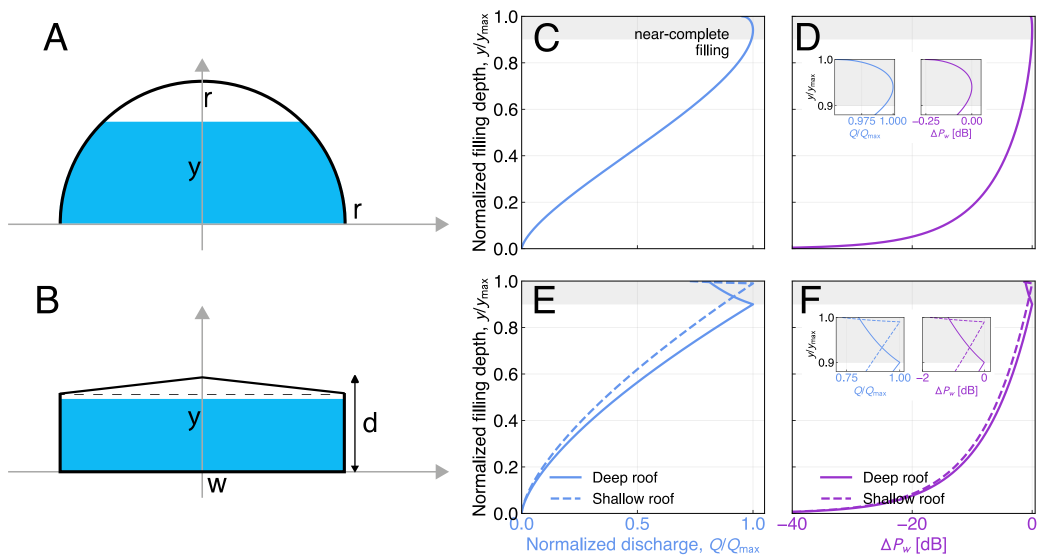

Figure 6: Roof-friction mechanism for glaciohydraulic tremor quieting during drainage pathway pressurization. (A–B) Idealized conduit geometries considered in the model: (A) a semi-circular R-channel and (B) a broad, low-aspect-ratio rooftop-shaped conduit. (C–F) Modeled changes in normalized discharge $Q/Q_{\max}$ and relative seismic power ΔP_w as a function of normalized filling depth y. Discharge is computed from the Darcy–Weisbach formulation, and seismic-power changes are estimated using the $P_w \propto Q^{5/4}$ scaling. Grey shading highlights the near-complete filling regime, where roof contact increases wetted perimeter and hydraulic resistance. Insets show the reduction in discharge and seismic power during this final transition toward pressurized flow.

5.4. Implications for water redistribution and stick-slip

The roof-friction mechanism implies that GHT quieting can occur while basal water pressure continues to rise. If near-complete filling temporarily reduces channelized discharge, the excess water must be transiently accommodated in subglacial or englacial storage, accessed via flow through hydraulically connected cavities and distributed drainage pathways.

The storage required by this redistribution is modest. Accommodating meltwater input over the $\sim$1 h pre-stick-slip quieting phase analyzed here, at a typical runoff of $\sim 10\,\mathrm{m^3\,s^{-1}}$, corresponds to $\sim 3.6\times10^4\,\mathrm{m^3}$. Distributed over the low-slope bed area upglacier of the measurement site ($\sim 1\,\mathrm{km^2}$, Fig. 1), this volume represents a water layer of $\sim$3.6 cm. The stored water layer can be translated into the change in hydraulic head (see the englacial storage formulation of equation 10 in Werder et al., 2013) using the storage fraction (englacial void ratio) taken as $e_v \approx 1\%$ typical of temperate Alpine glaciers (Huss et al., 2007; Werder et al., 2013). This yields a rise in hydraulic head of only $\sim$3.6 m (equivalent to $\sim$0.35 bar). The strength of the resulting gradient feedback on the constricted reach, and hence the process terminating individual quieting episodes, depends on the length over which the excess head is accommodated, which our observations do not uniquely determine. We propose that relating this length to the spatial extent of the MFP-derived source region is an interesting direction for future work. More generally, at temperate glaciers, proglacial discharge typically lags melt input by several hours, implying short-timescale storage. Such time lags are reproduced in subglacial drainage simulations using an englacial void ratio on the order of 10^{-2} (Werder et al., 2013), consistent with the value adopted here.

This redistribution carries an additional necessary condition: the hydraulic conductivity of the surrounding distributed drainage system must be comparable to that of the constricted channelized drainage element. If the distributed system was less conductive, the local pressure gradient across the constriction would instead increase, accelerating flow through the channel and consequently increasing rather than decreasing local discharge. This connectivity involves both lateral access from the constriction into the distributed system at the tremor site and access from the distributed system into the storage volume upglacier of the constriction, where the excess water is accommodated and where the borehole sensor records the associated pressurization. The occurrence of GHT quieting during rising basal water pressure suggests a hydraulically well-connected distributed system at this stage of the melt season, consistent with late-melt-season configurations in which channelized and distributed drainage components coexist and interact (Fountain and Walder, 1998; Werder et al., 2013; Flowers, 2015). The redistribution further implies that a spatially confined constriction, expressed through the MFP results as a $\sim$35 m $\times$ 40 m source region in the 10–20 Hz band, can control the pressurization and water distribution of a larger portion of the surrounding drainage system. The geometry of localized drainage elements may thus dictate the hydraulic and mechanical state of the bed at scales far exceeding the constriction itself.

As the drainage element approaches complete filling, turbulent channel flow weakens, reducing GHT power, while water pressure increases in adjacent parts of the drainage system, lowering the effective pressure and promoting enhanced basal motion (Iken and Bindschadler, 1986; Schoof, 2010;

Lipovsky and Dunham, 2017). The relationship between effective pressure and stick-slip behavior, however, is not straightforward. High effective pressure may favor the formation and unstable failure of velocity-weakening patches, for example through sediment entrainment and enhanced ice–bed contact (Lipovsky et al., 2019). Icequake observations at Saskatchewan Glacier show basal seismicity concentrated along hydrologically well-connected parts of a subglacial drainage network when local stresses on the remaining ice–bed contacts and debris–bed drag increase during cavity dilation (Stevens et al., 2024). These findings can be reconciled with observations at Rhône Glacier, where stick-slip tremor occurs during intervals of elevated basal water pressure and was proposed to be promoted by the associated reduction in effective pressure (Köpfli et al., 2022), through the spatial heterogeneity implied by our redistribution scenario: pressurized distributed drainage elements reduce effective pressure and accelerate sliding over part of the bed, while neighboring bed patches retain high effective pressure and velocity-weakening properties, acting as seismic asperities that fail in stick-slip mode as the surrounding bed unlocks. The effective-pressure control on stick-slip may depend on the spatial arrangement of drainage elements and on local interface properties, such as till or bed roughness.

The observed sequence supports the hypothesis that quieting, pressurization, and stick-slip are stages of a single hydraulic cycle. The high-frequency GHT quieting precedes the high-pressure interval and is followed by enhanced surface velocity, with the phase offset between basal water pressure and surface velocity reflecting an Iken-type response (Iken and Bindschadler, 1986). In particular, the onset of rising basal water pressure slightly precedes the quieting onset (Fig. 3), as expected if conduit filling under rising pressure precedes roof contact. The spatial proximity between GHT localizations and previously reported stick-slip tremor locations further suggests that hydraulic and mechanical processes occur in nearby basal regions (Fig. E.7).

GHT quieting, in this view, is not just a precursor to stick-slip but a seismic expression of the pressurized drainage state in the distributed system. Pressurization of the drainage pathway simultaneously suppresses turbulent seismic radiation (producing quieting) and reduces effective pressure on the surrounding bed (promoting stick-slip). The reappearance of quieting after stick-slip tremor stops, while pressure remains elevated (Fig. 2), supports this interpretation and suggests that quieting tracks the hydraulic state rather than the stick-slip process.

Because proglacial runoff shows no reduction at the scale of the daily melt cycle and because MFP locations remain present during quieting, the reduction in GHT power is unlikely to reflect reduced glacier-wide water input or a cessation of subglacial flow. Instead, it points to local drainage reorganization and pressure redistribution through connected cavities or distributed drainage elements. In this interpretation, the reduction in GHT power reflects reduced seismic radiation from turbulent water flow within the channelized component of the subglacial hydraulic system

5.5. Sources of uncertainty

Several factors limit how directly GHT quieting can be translated into hydraulic variables. Seismic power depends not only on discharge, but also on conduit geometry, hydraulic gradient, hydraulic radius, source coupling, source location, and propagation effects (Gimbert et al., 2016; Nanni et al., 2020; Aki and Richards, 2002). Using the roof-friction model to translate modeled discharge reductions into GHT-power changes is therefore a first-order estimation. In particular, these estimates rely on the assumption that seismic power responds primarily to the change in discharge and flow velocity, through the scaling $P_w \propto Q^{5/4}$, and neglect the concurrent increase in the wetted perimeter over which turbulent wall-pressure fluctuations (and seismic waves) are generated (Gimbert et al., 2016). This radiating boundary grows by up to a factor of two at roof contact in the flat-roof end-member, acting against the velocity-driven power reduction. The modeled ΔP_w values in Section 5.3 are therefore first-order estimates of the velocity-driven contribution to GHT quieting.

The modeled roof-friction geometries represent idealized end-member conduit shapes and do not resolve evolving roughness, bed material properties (e.g., deformable sediment), conduit closure, or time-dependent connectivity between channels and cavities. Other mechanisms may also contribute to the observed quieting, including a reduced hydraulic gradient during pressurization, as proposed by Köpfli et al. (2022). Although a reduction in the driving gradient during rising water pressure may appear counterintuitive, it can result from a backwater effect. When meltwater input exceeds the discharge capacity of downstream channels, water backs up in the upglacier direction, raising the hydraulic head along the backed-up reach and diminishing the head difference driving flow from upstream. Hence, the local hydraulic gradient and net channel flux diminish even as water pressure rises. These mechanisms are not mutually exclusive. Rather, they describe complementary aspects of the same process: water backing up behind a capacity-limited conduit reach both reduces the upstream hydraulic gradient (Köpfli et al., 2022) and drives the local filling and roof contact that increase frictional resistance (Section 5.3). Together, these effects could reduce turbulent seismic radiation during the quieting phase and contribute to the stronger quieting observed during individual events.

The Shreve-routing pathway (Shreve, 1972) provides a first-order estimate of likely drainage organization rather than an observation of instantaneous conduit geometry. This is particularly important because the flotation factor K likely varies in space and time, and because local drainage elements may transition between partially filled and pressurized states. The location of the main inferred pathway is, however, insensitive to the assumed pressure state persisting from $K = 0$ to $K = 1$ (Fig. E.1), so that this uncertainty affects the local hydraulic state along the pathway rather than its position.

Our observations also do not uniquely distinguish between a channelized drainage element or a linked-cavity system (Kamb, 1987; Walder, 1986). The redistribution interpretation additionally assumes that the transmissivity of the distributed system is comparable to that of the channelized constriction. The observed off-channel pressurization is consistent with this condition, but does not constrain it directly. The borehole pressure sensor provides a local measurement whose hydraulic connection to the active drainage system may vary in time. We can expect deviations between individual pressure and seismic-power records and we base our interpretation on the systematic relationship that emerges in the multi-event stack (Fig. 3).

The MFP analysis constrains the dominant coherent source location, but does not fully separate simultaneous hydraulic and stick-slip tremor during active slip. This may partly explain the secondary maxima visible during stick-slip periods in Fig. 5. In addition, although the MFP results support a basal or near-basal origin for the dominant coherent source, vertical resolution remains limited and englacial contributions cannot be fully ruled out.

Despite these limitations, the central observations remain robust: high-frequency GHT weakens while basal water pressure rises, coherent MFP localizations persist during quieting, and the spatial distribution of coherent seismic energy varies between periods. The amplitude decrease is strongest in the 10–20 Hz band, whereas the period-dependent spatial redistribution is most evident in the 6–8 Hz band. These frequency-dependent signatures indicate that local flow conditions control the generation of high-frequency seismic noise and, most likely, the redistribution of flow within the surrounding drainage system. These observations support the interpretation that GHT quieting reflects transient input of water from localized conduit into the surrounding distributed drainage system.

6. Conclusions

We investigated the quieting of glaciohydraulic tremor (GHT), expressed as a decrease in seismic power preceding stick-slip tremor at Rhône Glacier, by combining seismic and glaciological observations, matched-field processing, and physics-based hydraulic modeling. Quieting is strongest in the 10–20 Hz band, while the 6–8 Hz band shows a weaker decrease and a broader spatial distribution of coherent seismic energy. Matched-field processing indicates that coherent GHT sources persist during quieting near the inferred subglacial drainage pathway, showing that quieting reflects reduced seismic radiation from an active hydraulic source rather than disappearance of the source itself.

Our results show that GHT quieting does not track meltwater input alone: quieting occurs during rising basal water pressure and we interpret it as a transient change in drainage-system state. Near-complete filling and roof contact within broad, low-aspect-ratio drainage elements increase wetted perimeter and hydraulic resistance, temporarily reducing channelized discharge, flow velocity, and turbulent seismic radiation. This provides a physical mechanism by which GHT power can decrease even as basal water pressure rises.

These findings imply that basal slip and stick-slip activity cannot be assumed to scale directly with melt production or glacier-wide runoff. Rather, the onset of rapid motion also depends on the hydraulic state of the subglacial drainage system. Transitions from partially filled toward pressurized drainage conditions may redistribute water toward connected cavities or distributed drainage elements, reduce effective pressure over part of the bed, and promote abrupt changes in basal motion.

In particular, our observations suggest that localized flow-limiting drainage elements can act as switches for the wider drainage network: their transient pressurization redirects water into distributed drainage elements, lowering effective pressure over a broad bed area and conditioning the onset of rapid basal motion.

More broadly, the spectral and spatial organization of GHT can reveal short-lived drainage reorganization that is otherwise difficult to observe directly. GHT quieting may therefore act as a seismic indicator of threshold-like changes in hydraulic resistance and ice–water coupling at the bed. Future work should test whether similar quieting episodes occur in other glacier settings and combine tremor observations with direct pressure measurements and hydrological models to better resolve the transitions that control glacier sliding.

7. Acknowledgements

The Authors thank Daniel Farinotti for his co-supervision of N. Caldera master's internship, and Janneke van Ginkel for fruitful discussions. M.C. acknowledges support from the Poincaré fellowship program of the Observatoire de la Côte d'Azur (project SEISRIVER) and the European Research Council (ERC) under the European Union's Horizon Europe research and innovation programme (grant agreement ID: 101163251, UNREST). FG acknowledges funding from the European Research Council (ERC) under grant number 101126009 (REASSESS).

8. Author contributions

M. Chmiel: Conceptualization, Methodology, Formal Analysis, Software, Writing-Original draft preparation, Investigation, Supervision of N. Caldera; N. Caldera: Methodology, Software, Formal Analysis, Investigation; F. Gimbert: Conceptualization, Writing-Original draft preparation, Reviewing and Editing; G. Olivier: Conceptualization, Formal Analysis, Methodology, Investigation; A. Guadagnini: Supervision of N. Caldera, Reviewing and Editing; D. Gräff: Data curation, Reviewing and Editing; M. Köpfli: Reviewing and Editing, Data curation; M. Werder: Methodology, Formal Analysi, Reviewing and Editing; F. Walter: Conceptualization, Formal Analysis, Methodology, Resources, Supervision of N. Caldera, Reviewing and Editing, Data curation.

9. Declaration of generative AI and AI-assisted technologies in the manuscript preparation process

During the preparation of this work the authors used Claude (Anthropic) in order to assist with language editing and restructuring of the text. After using this tool, the authors reviewed and edited the content as needed and take full responsibility for the content of the published article.

10. Data Availability Statement

Data

Seismometer data from the 4D local glacier seismology network are archived at the Swiss Seismological Service and are openly available through the SED FDSN web services (`http://www.fdsn.org/networks/detail/4D_1985`, network code 4D, Swiss Seismological Service (SED) At ETH Zurich (1985)). Data sets for water pressure, ice flow velocity, bedrock topography, ice thickness, and station locations were sourced from the public repository accompanying Köpfli et al. (2022), available from ETH Zurich's Research Collection (`https://doi.org/10.3929/ethz-b-000569254`).

Code and data products

Code developed for this study is publicly available in our Zenodo repository (`10.5281/zenodo.15662929`). This includes example scripts for: hydraulic potential and upstream area calculation, source localization with the Bartlett Matched-Field Processing (MFP) method, and modeling channel discharge as a function of filling depth. The repository also contains the data products (MFP results, cross-correlation files, and dispersion curves).

Seismic data pre-processing was performed using the Obspy Python framework (`https://www.obspy.org`, Beyreuther et al. (2010)). Ambient noise cross-correlation analysis was conducted using MSNoise, which is available for download at `http://www.msnoise.org/`.

Figures

Figures 1A-C, 4A-B, and 5 were made using the perceptually-uniform "cmocean" colormaps for MATLAB (Thyng et al., 2016).

Appendix A. Preprocessing of the borehole data and noise correlations

Before calculating monthly noise correlations and locating noise sources with Matched-Field Processing (MFP), pre-processing is applied to each borehole station. The data are first corrected by the instrument sensitivity to convert the number of counts into the ground velocity. We downsample the data to 500 Hz since most of the background seismic energy (outside of stick-slip tremor times) is present below 300 Hz (Köpfli et al., 2022). Downsampling the borehole data from 2000 Hz to 500 Hz also accelerates the processing time and makes it possible to jointly use the borehole and the surface data that are sampled at 500 Hz with seismic interferometry and MFP.

Appendix A.1. 30 days noise correlations

We perform cross-correlation of one month of seismic data using a time window of 5 minutes and a maximum time lag of 8 seconds. The cross-correlation procedure follows the method proposed by Bensen et al. (2007), which includes spectral whitening and one-bit normalization before calculating the cross-correlations. These steps are implemented in the Python package MSNoise (Lecocq et al., 2014).

Appendix B. Matched-Field Processing (MFP)

Matched-Field Processing (MFP) is an extension of a traditional plane-wave beamformer (Kuperman and Turek, 1997) that can be applied to any complex medium, as long as spatially coherent phase information can be extracted between nearby sensors. The general idea of beamforming in seismology is to estimate the coherent portion of seismic wave energy that propagates over the seismic array and to determine its propagation characteristics (e.g., Rost and Thomas, 2002). In the general case, the phase information at frequency ω is obtained from a data vector $\mathbf{d}(\omega)$ that consists of the discrete Fourier transforms of each station record:

$$\mathbf{d}(\omega) = [d_1(\omega), d_2(\omega), \ldots, d_N(\omega)] \tag{B.1}$$

where N is the number of stations within the array.

The Cross-Spectral Density Matrix (CSDM), $\mathbf{K}(\omega)$, captures the relative phase differences between the stations and is typically calculated by averaging M data vectors over a time window T:

$$\mathbf{K}(\omega) = \frac{1}{M} \sum_{i=1}^{M} \mathbf{d}_i(\omega)\, \mathbf{d}_i^H(\omega) \tag{B.2}$$

where H denotes the Hermitian (conjugate transpose).

The synthetic wavefield from a point-like source is modeled using a frequency-domain Green's function that depends on the source spatial coordinates x, y, and z, and the medium's homogeneous phase velocity c:

$$\mathbf{d}(\omega, \mathbf{r}_{xyz}) = \exp\left(\frac{i\omega r_{xyz}}{c}\right) \tag{B.3}$$

where r_{xyz} is the distance between each station in the array and the trial source location.

The phase velocity c is optimized using MFP output over a time window T of 5 minutes. To determine the final optimized phase velocity, seven time windows are randomly sampled across the monitoring period. For each time window, we search for the source position yielding the maximum phase coherence (Fig. E.8). The final optimized phase velocity is calculated as the average, yielding $c_{\text{final}} = 1800\,\text{ms}^{-1}$.

To map the source locations in space, we use the linear Bartlett processor due to its robustness (Chmiel et al., 2016):

$$B_{\text{Bartlett}}(\omega, \mathbf{r}_{xyz}) = \sum_{\omega} \left| \mathbf{d}^H(\omega, \mathbf{r}_{xyz})\, \mathbf{K}(\omega)\, \mathbf{d}(\omega, \mathbf{r}_{xyz}) \right| \tag{B.4}$$

B_{Bartlett} values range from 0 to 1, with higher values indicating greater phase coherence. Physically, the Bartlett processor corresponds to a cross-correlation between the recorded and modeled wavefields. As a linear, phase-based method, its spatial resolution is limited by diffraction laws and wavelength, though it is robust for source detection.

Appendix B.1. Source localization with MFP

For source localization, we use a time window T of 5 min to calculate the CSDM, averaging 30 data vectors of 10 s. The averaging over multiple short data vectors should improve the coherency retrieved with the CSDM (Seats et al., 2012). For each frequency band, we averaged the MFP output over 20 individual frequencies.

We use the vertical component of 8 seismic stations for the 3D MFP localization: 3 surface stations (RA81, RA82, and RA87) and 5 boreholes stations (RA91A, RA91B, RA92A, RA93A, RA93B). We constrain the search with the minimization algorithm to the x, y, and z space: for xy, the dimensions of the search area are limited to the minimum and maximum x, y coordinates of the seismic stations used for localization. For the depth z, we use the a priori information on the glacier bed depth and geometry and constrain the search to altitudes between 2294 m and 2334 m a.s.l. that contains the glacier bed topography variations for the specified xy search area. We assume that the algorithm correctly converges if the optimal location is within the grid xy, with localization at the xy borders being excluded. Due to poorer resolution at depth, we reject locations at the upper z-limit to avoid polluting the results with possible surface and englacial sources.

To maximize the efficiency of our algorithm and map secondary seismic sources, we use a direct minimization algorithm (Lagarias et al., 1998; Nelder and Mead, 1965) to converge to the best match between the modeled and the observed phase delays rather than exhaustive grid-search exploration. The convergence criterion is reached if the solver reaches its lower bound on the size of the step in space and on the change in the MFP values, which is set to 1e-4, with a maximum of 600 iterations.

The Nelder-Mead optimization requires an initial guess of the optimal location. We follow two strategies for this initial guess:

1. We first calculate the MFP output using a 3D grid search over easting, northing, and depth (x, y, and z) with the previously optimized phase velocity. This approach yields a 3D cube containing the MFP output for each point on the grid. The optimal location of a dominant source is identified as the argument of the maximum of the MFP output, and we define this position as the initial guess for the Nelder–Mead optimization. This approach enables us to explore the global maximum in the 10–20 Hz frequency band.

2. Following Nanni et al. (2022), we also tested MFP localization in the 6–8 Hz frequency band using multiple starting points to investigate possible local maxima associated with simultaneous activity from multiple sources. We further verified that the dominant source region in the 10–20 Hz band is unchanged when using multiple starting points, which indicated that the localization is robust to the choice of initial point (Fig. E.9).

Appendix B.2. Computation of normalized weighted MFP density

To compare the spatial distribution of MFP localizations between periods and frequency bands, we converted the quality-controlled source locations into normalized weighted density maps. For each 5 min MFP window, we retained the optimized source locations and their corresponding MFP output values. Localizations were excluded if they occurred on the horizontal boundaries of the search grid, on the upper vertical boundary, or if their MFP output was lower than the random-coherence level $1/N$, where N is the number of stations used in the MFP analysis. The remaining 3D localizations were projected onto the horizontal plane and binned into a regular $5\,\mathrm{m} \times 5\,\mathrm{m}$ grid. For each grid cell i, we summed the MFP output values of all localizations falling within that cell and normalized by the total summed MFP output over the full grid:

$$D_i = \frac{\sum_{j \in i} B_j}{\sum_{j=1}^{M} B_j}, \tag{B.5}$$

where D_i is the normalized weighted MFP density in grid cell i, B_j is the MFP output value of localization j, and M is the total number of retained localizations for the considered period and frequency band. The resulting maps therefore show the relative spatial concentration of coherent MFP detections, weighted by localization strength.

Appendix B.3. Grid definition and starting point selection for localization

We use the location associated with the maximum 3D MFP output from the first analyzed 5-minute time window (on July 22, 00:00 UTC) as the initial guess for the Nelder–Mead optimization. To explore potential secondary seismic sources in 6-8 Hz, we defined 4 starting points at distances of $1\times$ and $2 \times \lambda/2$ (half the seismic wavelength) in both x and y directions from the location of the main source. The Bartlett processor is a phase-based linear algorithm, and its spatial accuracy is limited by diffraction laws. This resolution limit is expected to be approximately $\lambda/2$, where λ is the wavelength of the signal. For the 6–8 Hz frequency band and assuming a phase velocity of 1800 m/s, $\lambda/2 \approx 120$ m. The spacing of $\lambda/2$ between the starting points enables us to distinguish between spatially separate sources and reduces the likelihood of re-identifying the same source.

Appendix C. Supplementary figures

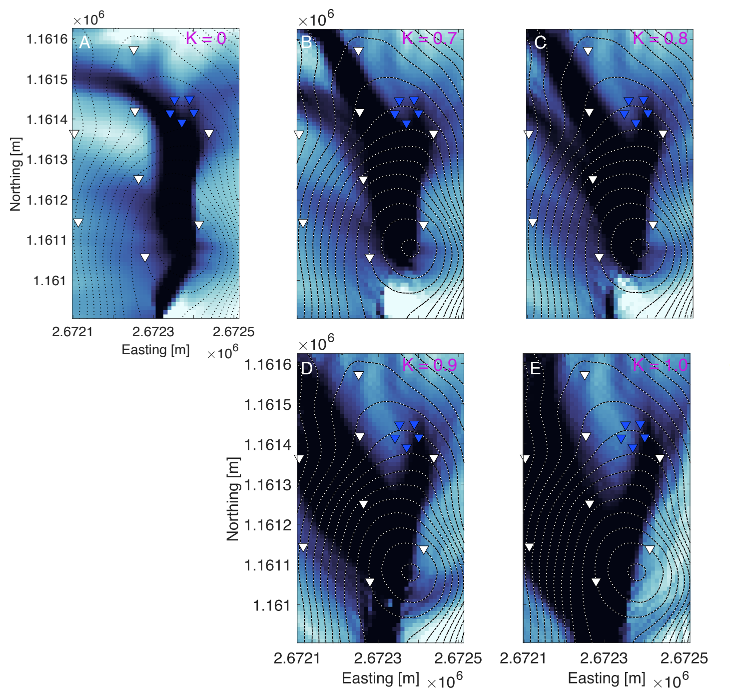

Figure E.1: Sensitivity of hydraulic-potential routing to flotation factor K. Upstream area was calculated for K = 0, 0.7, 0.8, 0.9, and 1.0 (A–E), where $K = 0$ corresponds to purely topography-controlled routing and $K = 1$ to water pressure equal to ice overburden pressure. Dotted contours show bed elevation interpolated from ground-penetrating radar surveys. White and blue triangles mark surface and borehole seismic stations, respectively. Colors show $\log_{10}$ upstream area, with displayed values ranging from 1 to 2.2.

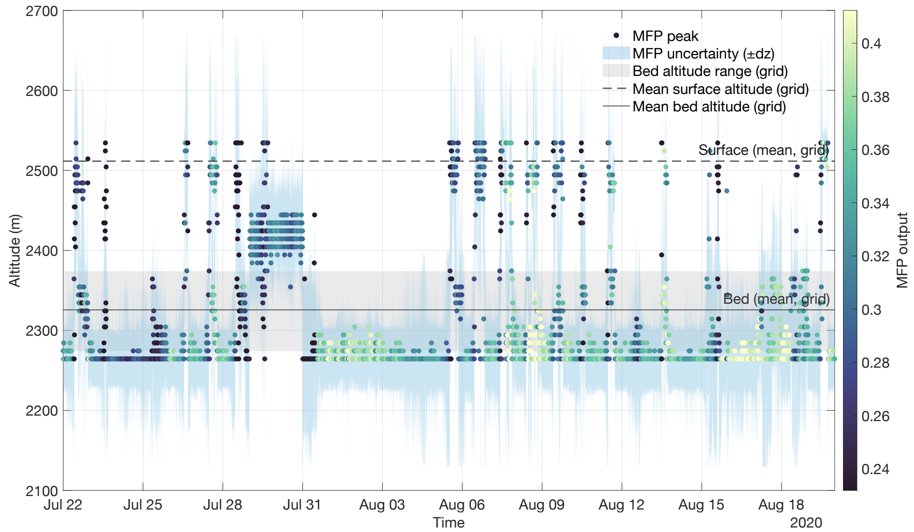

Figure E.2: Altitude of the maximum matched-field processing (MFP) output for 5 min time windows in the 10–20 Hz band between 22 July and 19 August 2020. Points show the altitude of the MFP peak, colored by MFP output. Light blue vertical envelopes indicate the vertical extent of the high-coherence region, defined here by locations with MFP output ≥90% of the peak value for each time window. The gray band shows the range of radar-derived bed elevations within the MFP search area, while horizontal lines indicate the mean bed and surface elevations within the same area. Most MFP maxima cluster near the radar-derived bed, motivating the vertically constrained MFP search used for the spatial localization analysis.

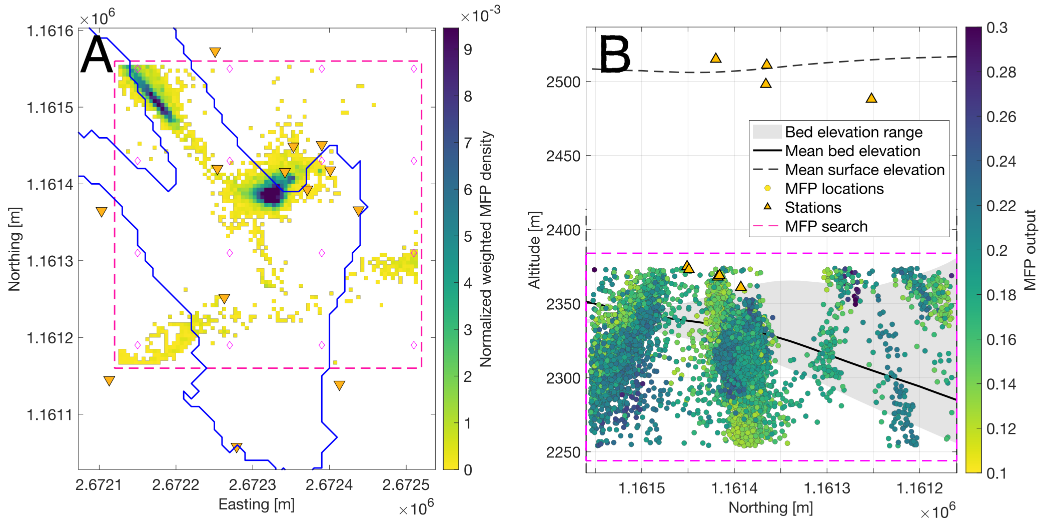

Figure E.3: Full-array MFP localization in the 6–8 Hz band (outside of stick-slip tremor times). (A) Normalized weighted MFP-density map computed using all available stations, including 5 borehole seismometers and 8 surface seismometers. Blue contours indicate the inferred subglacial drainage pathway, triangles mark seismometers, and the magenta dashed box shows the horizontal MFP search area. (B) Northing-altitude projection of the corresponding MFP localizations, colored by MFP output. The grey band shows the radar-derived bed-elevation range, black and grey dashed lines show the mean bed and surface elevations, respectively, and the magenta dashed box marks the vertical MFP search domain. The full-array result shows coherent energy concentrated near the inferred drainage pathway and close to the radar-derived bed, supporting the robustness of the main MFP localization pattern. Additional maxima outside the central drainage area may reflect additional less coherent subglacial and englacial sources.

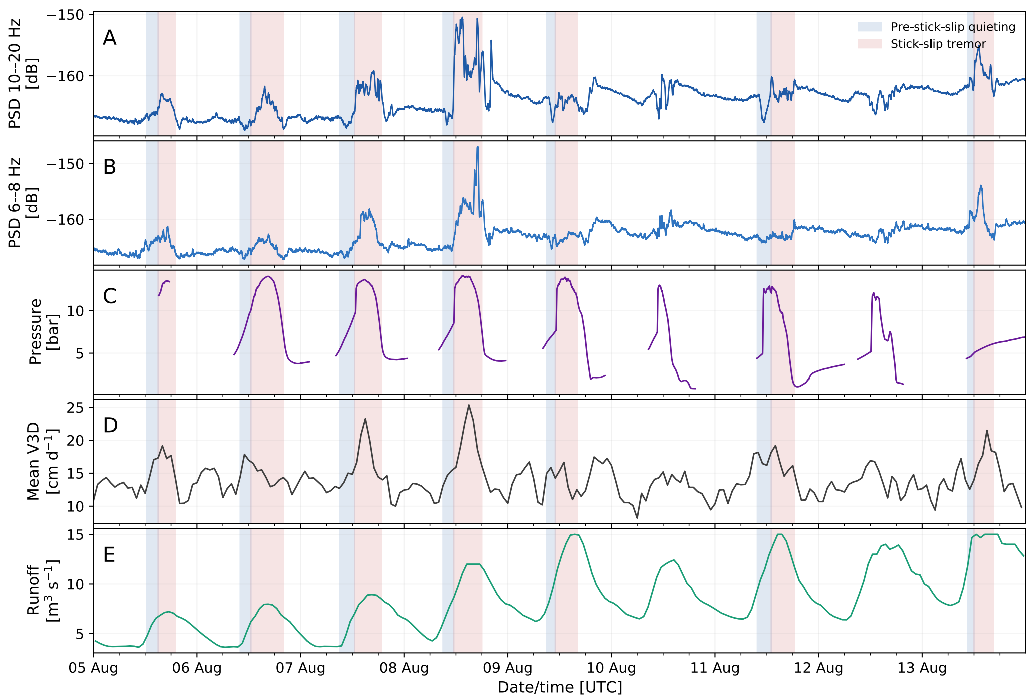

Figure E.4: Continuous seismic and hydrological observations from 5 to 13 August 2020. (A–B) Smoothed PSD in the 10–20 Hz and 6–8 Hz bands. (C) Basal water pressure, shown only during intervals with available measurements. (D) Mean 3-D surface velocity from GNSS stations PPM3 and PPM4. (E) Proglacial runoff. Blue shading marks the pre-stick-slip quieting interval, red shading marks stick-slip tremor as detected by Köpfli et al. (2022).

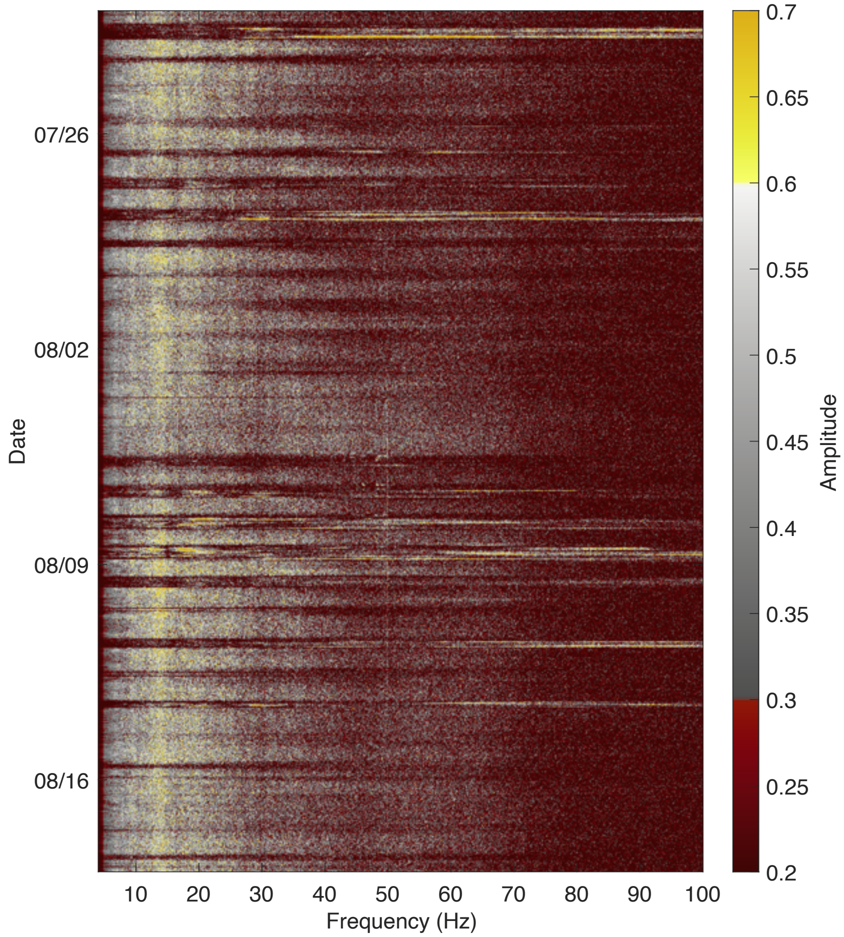

Figure E.5: Spectrogram of the acausal part of noise correlations between two borehole stations RA91A and RA93A over 1 month.

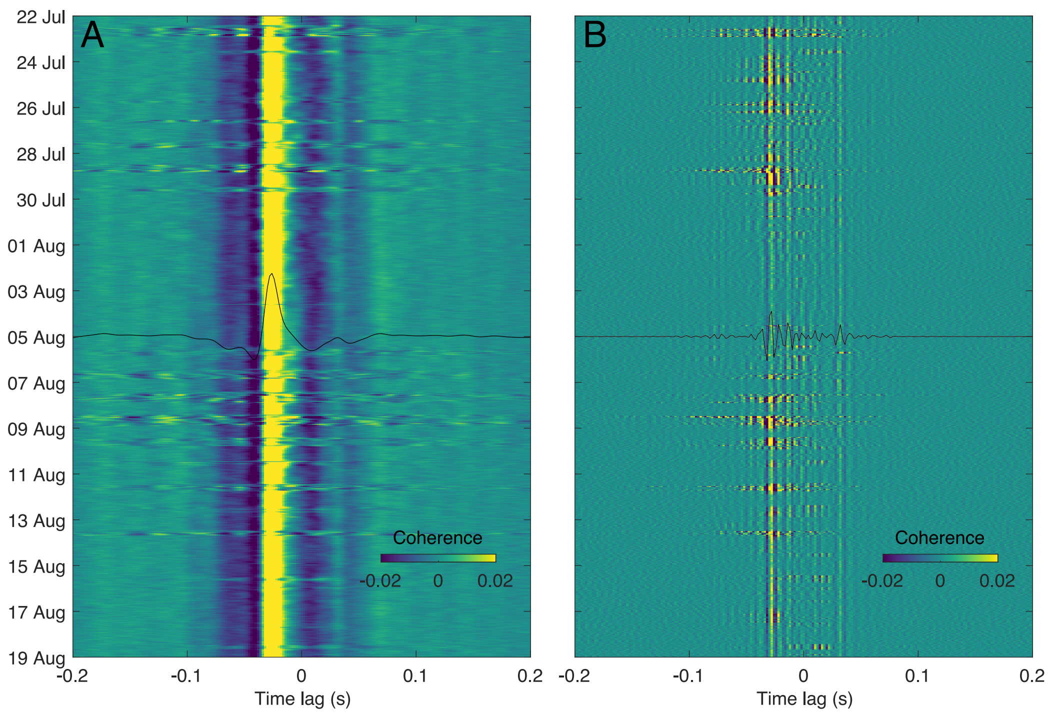

Figure E.6: Noise correlations between two borehole stations RA91A and RA93A in low frequencies (6-49 Hz) and high frequencies (100-200 Hz) over 1 month. The average stack of all noise correlations is plotted in the middle of each figure.

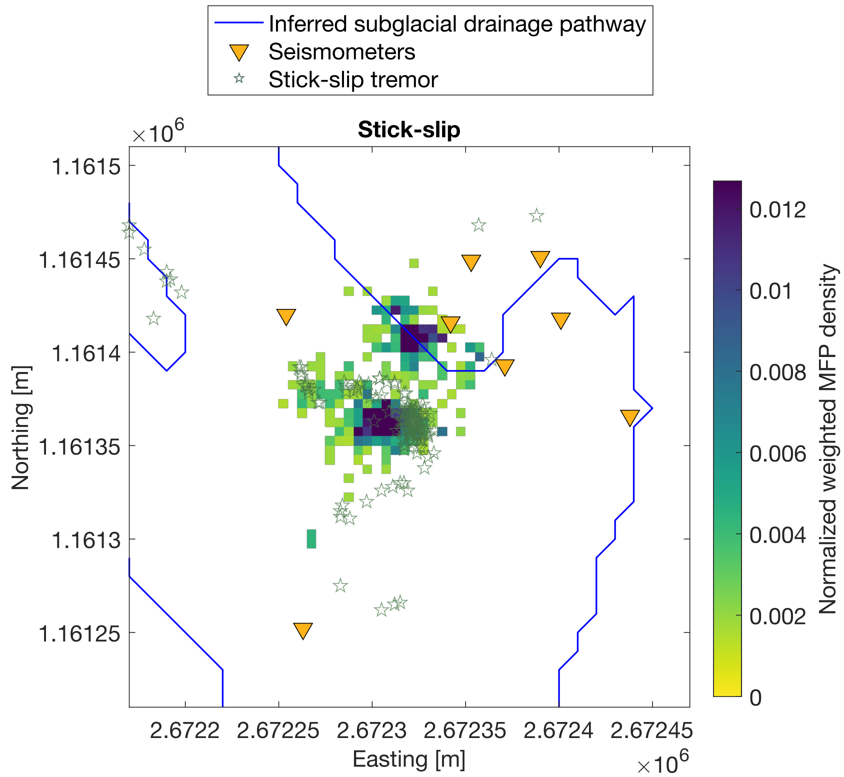

Figure E.7: Comparison between 10-20 Hz GHT localization and stick-slip tremor locations. Normalized weighted MFP density in the 10–20 Hz band during the stick-slip period, with independently identified stick-slip tremor locations overlaid as stars. The blue line indicates the inferred subglacial drainage pathway from Shreve routing, and inverted triangles mark seismic stations. The strongest MFP-density regions lie near the inferred drainage pathway and partly overlap with the stick-slip tremor locations, indicating that high-frequency GHT and stick-slip tremor originate from nearby basal regions. This spatial overlap does not uniquely separate simultaneous hydraulic tremor from stick-slip-generated energy during active slip.

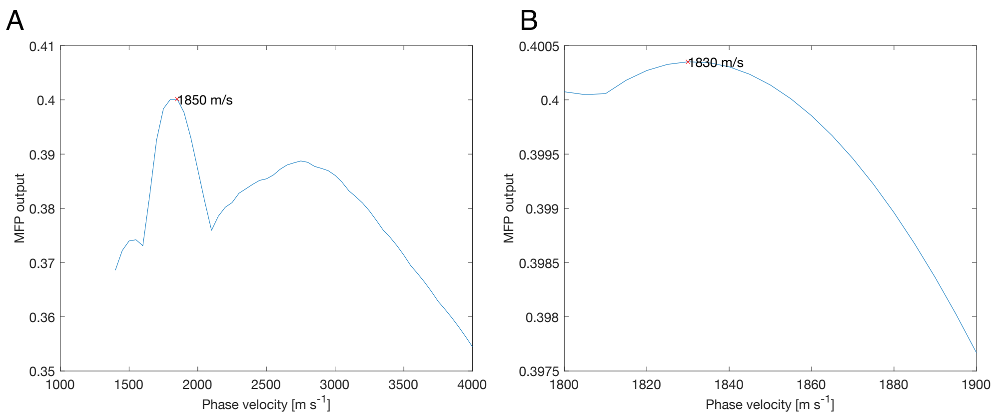

Figure E.8: Two-step phase velocity optimization approach based on MFP output, demonstrated using a 5-minute time window on August 8 at 14:15 UTC in the 10–20 Hz range. A. 4D grid search over x, y, z, and c using a "coarse" phase velocity vector ranging from 1400 to 4000 ms^{-1}, with increments of 50 ms^{-1}. B. A secondary search using a "fine" phase velocity vector around the optimal velocity identified in the first search, $\pm$50 ms^{-1}, with increments of 5 ms^{-1}. Phase velocities corresponding to the maximum MFP output are indicated by red crosses.

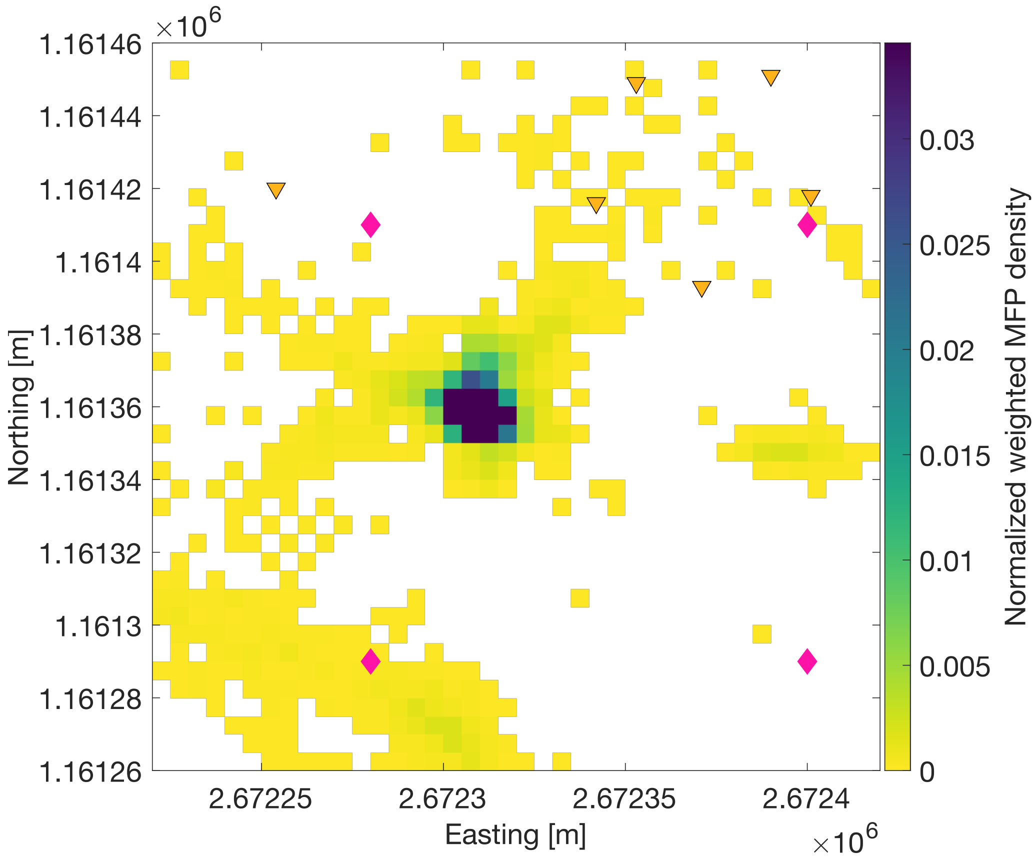

Figure E.9: Same analysis as in Figure 5A, but with multiple MFP optimization starting points following Nanni et al. (2021). Magenta diamonds mark the starting points. The dominant source region is unchanged, indicating that the localization is robust to the choice of initial starting point.

References

Aki, K., Richards, P., 2002. Quantitative Seismology. University Science Books. URL: `https://books.google.fr/books?id=sRhawFG5_EcC`.

Andrews, L.C., Catania, G.A., Hoffman, M.J., Gulley, J.D., Lüthi, M.P., Ryser, C., Hawley, R.L., Neumann, T.A., 2014. Direct observations of evolving subglacial drainage beneath the Greenland Ice Sheet. Nature 514, 80–83. URL: https://www.nature.com/articles/nature13796, doi:10.1038/nature13796. number: 7520 Publisher: Nature Publishing Group.

Bartholomaus, T.C., Amundson, J.M., Walter, J.I., O'Neel, S., West, M.E., Larsen, C.F., 2015. Subglacial discharge at tidewater glaciers revealed by seismic tremor. Geophysical Research Letters 42, 6391–6398. doi:https://doi.org/10.1002/2015GL064590.

Bauder, A., Huss, M., Linsbauer, A., 2020. The Swiss glaciers 2017/18 and 2018/19. Glaciological Report 139/140. Swiss Academy of Sciences (SCNAT). doi:http://doi.org/10.18752/glrep139-140.

Bensen, G.D., Ritzwoller, M.H., Barmin, M.P., Levshin, A.L., Lin, F., Moschetti, M.P., Shapiro, N.M., Yang, Y., 2007. Processing seismic ambient noise data to obtain reliable broad-band surface wave dispersion measurements. Geophysical Journal International 169, 1239–1260. doi:10.1111/j.1365-246X.2007.03374.x.

Beyreuther, M., Barsch, R., Krischer, L., Megies, T., Behr, Y., Wassermann, J., 2010. Obspy: A python toolbox for seismology. Seismological Research Letters 81, 530–533. doi:10.1785/gssrl.81.3.530.

Boulton, G.S., 1972. Modern Arctic glaciers as depositional models for former ice sheets. Journal of the Geological Society 128, 361–393. URL: https://www.lyellcollection.org/doi/abs/10.1144/

gsjgs.128.4.0361, doi:10.1144/gsjgs.128.4.0361. publisher: The Geological Society of London.

Burtin, A., Bollinger, L., Vergne, J., Cattin, R., Nábělek, J.L., 2008. Spectral analysis of seismic noise induced by rivers: A new tool to monitor spatiotemporal changes in stream hydrodynamics. Journal of Geophysical Research: Solid Earth 113. doi:https://doi.org/10.1029/2007JB005034.

Canassy, P.D., Röösli, C., Walter, F., 2016. Seasonal variations of glacier seismicity at the tongue of Rhonegletscher (Switzerland) with a focus on basal icequakes. Journal of Glaciology 62, 18–30. doi:10.1017/jog.2016.3.

Chmiel, M., Roux, P., Bardainne, T., 2016. Extraction of phase and group velocities from ambient surface noise in a patch-array configuration. Geophysics 81, KS231–KS240. doi:10.1190/geo2016-0027.1.

Chmiel, M., Roux, P., Bardainne, T., 2019. High-sensitivity microseismic monitoring: Automatic detection and localization of subsurface noise sources using matched-field processing and dense patch arrays. Geophysics 84, KS211–KS223. doi:10.1190/geo2018-0537.1.

Chmiel, M., Walter, F., Pralong, A., Preiswerk, L., Funk, M., Meier, L., Brenguier, F., 2023. Seismic Constraints on Damage Growth Within an Unstable Hanging Glacier. Geophysical Research Letters 50, e2022GL102007. doi:10.1029/2022GL102007. _eprint: https://onlinelibrary.wiley.com/doi/pdf/10.1029/2022GL102007.

Chow, V., Maidment, D., Mays, L., 1988. Applied Hydrology. 1st edition ed., McGraw-Hill Science/Engineering/Math, New York.

Church, G., Bauder, A., Grab, M., Maurer, H., 2021. Ground-penetrating radar imaging reveals glacier's drainage network in 3D. The Cryosphere 15, 3975–3988. URL: https://tc.copernicus.org/articles/15/3975/2021/, doi:10.5194/tc-15-3975-2021. publisher: Copernicus GmbH.

Clarke, G.K.C., 1987. Fast glacier flow: Ice streams, surging, and tidewater glaciers. Journal of Geophysical Research: Solid Earth 92, 8835–8841. URL: https://agupubs.onlinelibrary.wiley.com/doi/abs/10.1029/JB092iB09p08835, doi:10.1029/JB092iB09p08835. publisher: John Wiley & Sons, Ltd.

Clyne, E., Alley, R.B., Vore, M., Gräff, D., Anandakrishnan, S., Walter, F., Sergeant, A., 2023. Glacial hydraulic tremor on Rhonegletscher, Switzerland. Journal of Glaciology 69, 370–380. URL: https://www.cambridge.org/core/journals/journal-of-glaciology/article/glacial-hydraulic-tremor-on-rhonegletscher-switzerland/4C2BB54BB742D13E1ADDCBE9E57EA770, doi:10.1017/jog.2022.69.

Cuffey, K.M., Paterson, W.S.B., 2010. The Physics of Glaciers. 4th ed., Academic Press, Amsterdam, Boston, Heidelberg, London, New York, Oxford, Paris, San Diego, San Francisco, Singapore, Sydney, Tokyo.

Faillettaz, J., Funk, M., Sornette, D., 2011. Icequakes coupled with surface displacements for predicting glacier break-off. Journal of Glaciology 57, 453–460. doi:10.3189/002214311796905668.

Flowers, G.E., 2015. Modelling water flow under glaciers and ice sheets. Proceedings of the Royal Society A: Mathematical, Physical and Engineering Sciences 471, 20140907. URL: https://royalsocietypublishing.org/doi/10.1098/rspa.2014.0907, doi:10.1098/rspa.2014.0907. publisher: Royal Society.

Fountain, A., Walder, J., 1998. Water flow through temperate glaciers. Reviews of Geophysics - REV GEOPHYS 36. doi:10.1029/97RG03579.

Fowler, A.C., 1987. Sliding with Cavity Formation. Journal of Glaciology 33, 255–267. URL: https://www.cambridge.org/core/journals/journal-of-glaciology/article/sliding-with-cavity-formation/672DBC2A9074FD7F8973C0651B6E2DBA, doi:10.3189/S0022143000008820.

Freeman, T., 1991. Calculating catchment area with divergent flow based on a regular grid. "Computers & Geosciences" 17, 413–422. URL: https://www.sciencedirect.com/science/article/pii/009830049190048I, doi:https://doi.org/10.1016/0098-3004(91)90048-I.

Gimbert, F., Tsai, V.C., Amundson, J.M., Bartholomaus, T.C., Walter, J.I., 2016. Subseasonal changes observed in subglacial channel pressure, size, and sediment transport. Geophysical Research Letters 43, 3786–3794. URL: https://onlinelibrary.wiley.com/doi/abs/10.1002/2016GL068337, doi:10.1002/2016GL068337. _eprint: https://onlinelibrary.wiley.com/doi/pdf/10.1002/2016GL068337.

Gimbert, F., Tsai, V.C., Lamb, M.P., 2014. A physical model for seismic noise generation by turbulent flow in rivers. Journal of Geophysical Research: Earth Surface 119, 2209–2238.

Grab, M., Mattea, E., Bauder, A., Huss, M., Rabenstein, L., Hodel, E., Linsbauer, A., Langhammer, L., Schmid, L., Church, G., Hellmann, S., Délèze, K., Schaer, P., Lathion, P., Farinotti, D., Maurer, H., 2021. Ice thickness distribution of all Swiss glaciers based on extended ground-penetrating radar data and glaciological modeling. Journal of Glaciology 67, 1074–1092. doi:10.1017/jog.2021.55.

Gräff, D., 2021. Small-Scale Processes at the Glacier Bed: Stick-Slip, Crack Waves and Sliding from Surface and Borehole Observations. Ph.D. thesis. ETH Zurich. URL: https://www.research-collection.ethz.ch/handle/20.500.11850/524634, doi:10.3929/ethz-b-000524634.

Gräff, D., Walter, F., 2021. Changing friction at the base of an Alpine glacier. Scientific Reports 11, 10872. doi:10.1038/s41598-021-90176-9. publisher: Nature Publishing Group.

Helmstetter, A., Nicolas, B., Comon, P., Gay, M., 2015. Basal icequakes recorded beneath an Alpine glacier (Glacier d'Argentière, Mont Blanc, France): Evidence for stick-slip motion? Journal of Geophysical Research: Earth Surface 120, 379–401. URL: https://onlinelibrary.wiley.com/doi/abs/10.1002/2014JF003288, doi:10.1002/2014JF003288. _eprint: https://onlinelibrary.wiley.com/doi/pdf/10.1002/2014JF003288.

Hewitt, I.J., Schoof, C., Werder, M.A., 2012. Flotation and free surface flow in a model for subglacial drainage. part 2. channel flow. Journal of Fluid Mechanics 702, 157–187. doi:10.1017/jfm.2012.166.

Hooke, R., Laumann, T., Kohler, J., 1990. Subglacial Water Pressures and the Shape of Subglacial Conduits. Journal of Glaciology - J GLACIOLOGY 36, 67–71. doi:10.1017/S0022143000005566.

Hooke, R.L., 1984. On the role of mechanical energy in maintaining subglacial water conduits at atmospheric pressure. Journal of Glaciology 30, 180–187. doi:10.3189/S0022143000005918.

Huss, M., Bauder, A., Werder, M., Funk, M., Hock, R., 2007. Glacier-dammed lake outburst events of gornersee, switzerland. Journal of Glaciology 53, 189–200. doi:10.3189/172756507782202784.

Iken, A., Bindschadler, R.A., 1986. Combined measurements of subglacial water pressure and surface velocity of findelengletscher, switzerland: Conclusions about drainage system and sliding mechanism. Journal of Glaciology 32, 101–119. doi:10.3189/S0022143000006936.

Iken, A., H, R., K, H., 1976. Deep Drilling With A Hot Water Jet. Z. GLETSCHERKDE GLAZIOLGEOL 12.

Kamb, B., 1987. Glacier surge mechanism based on linked cavity configuration of the basal water conduit system. Journal of Geophysical Research: Solid Earth 92, 9083–9100. URL: https://onlinelibrary.wiley.com/doi/abs/10.1029/JB092iB09p09083, doi:10.1029/JB092iB09p09083. _eprint: https://onlinelibrary.wiley.com/doi/pdf/10.1029/JB092iB09p09083.

Kuperman, W., Turek, G., 1997. Matched field acoustics. Mechanical Systems and Signal Processing 11, 141–148. doi:https://doi.org/10.1006/mssp.1996.0066.

Köpfli, M., Gräff, D., Lipovsky, B.P., Selvadurai, P.A., Farinotti, D., Walter, F., 2022. Hydraulic conditions for stick-slip tremor beneath an alpine glacier. Geophysical Research Letters 49, e2022GL100286. doi:https://doi.org/10.1029/2022GL100286.

Lagarias, J., Reeds, J., Wright, M.H., Wright, P.E., 1998. Convergence Properties of the Nelder-Mead Simplex Method in Low Dimensions. SIAM Journal on Optimization .

Lecocq, T., Caudron, C., Brenguier, F., 2014. MSNoise, a Python Package for Monitoring Seismic Velocity Changes Using Ambient Seismic Noise. Seismological Research Letters 85, 715–726. doi:10.1785/0220130073.

Lindner, F., Walter, F., Laske, G., Gimbert, F., 2020. Glaciohydraulic seismic tremors on an alpine glacier. The Cryosphere 14, 287–308. doi:10.5194/tc-14-287-2020.

Lipovsky, B.P., Dunham, E.M., 2017. Slow-slip events on the Whillans Ice Plain, Antarctica, described using rate-and-state friction as an ice stream sliding law. Journal of Geophysical Research: Earth Surface 122, 973–1003. URL: https://onlinelibrary.wiley.com/doi/abs/10.1002/2016JF004183, doi:10.1002/2016JF004183. _eprint: https://onlinelibrary.wiley.com/doi/pdf/10.1002/2016JF004183.

Lipovsky, B.P., Meyer, C.R., Zoet, L.K., McCarthy, C., Hansen, D.D., Rempel, A.W., Gimbert, F., 2019. Glacier sliding, seismicity and sediment entrainment. Annals of Glaciology 60, 182–192. doi:10.1017/aog.2019.24.

Lliboutry, L., 1968. General Theory of Subglacial Cavitation and Sliding of Temperate Glaciers. Journal of Glaciology 7, 21–58. doi:10.3189/S0022143000020396.

Mikesell, T.D., van Wijk, K., Haney, M.M., Bradford, J.H., Marshall, H.P., Harper, J.T., 2012. Monitoring glacier surface seismicity in time and space using Rayleigh waves. Journal of Geophysical Research: Earth Surface 117. URL: https://onlinelibrary.wiley.com/doi/abs/10.1029/2011JF002259, doi:10.1029/2011JF002259. _eprint: https://onlinelibrary.wiley.com/doi/pdf/10.1029/2011JF002259.

Nakata, N., Gualtieri, L., Fichtner, A. (Eds.), 2019. Seismic Ambient Noise. Cambridge University Press, Cambridge. URL: https://www.cambridge.org/core/books/seismic-ambient-noise/6D9AE0CC68897330A27DB7FF92ABAACF, doi:10.1017/9781108264808.

Nanni, U., Gimbert, F., Roux, P., Lecointre, A., 2021. Observing the subglacial hydrology network and its dynamics with a dense seismic array. Proceedings of the National Academy of Sciences 118, e2023757118. URL: https://www.pnas.org/doi/10.1073/pnas.2023757118, doi:10.1073/pnas.2023757118. publisher: Proceedings of the National Academy of Sciences.

Nanni, U., Gimbert, F., Vincent, C., Gräff, D., Walter, F., Piard, L., Moreau, L., 2020. Quantification of seasonal and diurnal dynamics of subglacial channels using seismic observations on an Alpine glacier. The Cryosphere 14, 1475–1496. URL: https://tc.copernicus.org/articles/14/1475/2020/, doi:10.5194/tc-14-1475-2020. publisher: Copernicus GmbH.

Nanni, U., Roux, P., Gimbert, F., Lecointre, A., 2022. Dynamic imaging of glacier structures at high-resolution using source localization with a dense seismic array. Geophysical Research Letters 49, e2021GL095996. doi:https://doi.org/10.1029/2021GL095996.

Nelder, J.A., Mead, R., 1965. A Simplex Method for Function Minimization. The Computer Journal 7, 308–313. doi:10.1093/comjnl/7.4.308.

Nolan, M., Echelmeyer, K., 1999. Seismic detection of transient changes beneath Black Rapids Glacier, Alaska, U.S.A.: I. Techniques and observations. Journal of Glaciology 45, 119–131. doi:10.3189/S0022143000003105.

Nye, J.F., 1965. The Flow of a Glacier in a Channel of Rectangular, Elliptic or Parabolic Cross-Section. Journal of Glaciology 5, 661–690. URL: https://www.cambridge.org/core/journals/journal-of-glaciology/article/flow-of-a-glacier-in-a-channel-of-rectangular-elliptic-or-parabolic-crosssectio F6D08A79AFF029EE34095241ECC6A360, doi:10.3189/S0022143000018670.

Ogier, C., 2024. Towards a better understanding of uncommon glacier outburst floods. Doctoral thesis. ETH Zürich. doi:https://doi.org/10.3929/ethz-b-000711790.

Podolskiy, E.A., Walter, F., 2016. Cryoseismology. Reviews of Geophysics 54, 708–758. doi:https://doi.org/10.1002/2016RG000526.

Rost, S., Thomas, C., 2002. Array Seismology: Methods and Applications. Reviews of Geophysics 40, 2–1–2–27. URL: https://onlinelibrary.wiley.com/doi/abs/10.1029/2000RG000100, doi:10.1029/2000RG000100. _eprint: https://onlinelibrary.wiley.com/doi/pdf/10.1029/2000RG000100.

Rutishauser, A., Maurer, H., Bauder, A., 2016. Helicopter-borne ground-penetrating radar investigations on temperate alpine glaciers: A comparison of different systems and their abilities for bedrock mapping. Geophysics 81, WA119–WA129. URL: https://doi.org/10.1190/geo2015-0144.1, doi:10.1190/geo2015-0144.1, arXiv:https://pubs.geoscienceworld.org/seg/geophysics/article-pdf/81/1/WA119/324

Röthlisberger, H., 1972. Water Pressure in Intra- and Subglacial Channels. Journal of Glaciology 11, 177–203. URL: https://www.cambridge.org/core/journals/journal-of-glaciology/article/water-pressure-in-intra-and-subglacial-channels/63F384A0C25D8CAD2928ABB06D812291, doi:10.3189/S0022143000022188.

Schoof, C., 2010. Ice-sheet acceleration driven by melt supply variability. Nature 468, 803–806. doi:10.1038/nature09618.

Schuler, T.V., Fischer, U.H., 2009. Modeling the diurnal variation of tracer transit velocity through a subglacial channel. Journal of Geophysical Research: Earth Surface 114. URL: https://onlinelibrary.wiley.com/doi/abs/10.1029/2008JF001238, doi:10.1029/2008JF001238. _eprint: https://onlinelibrary.wiley.com/doi/pdf/10.1029/2008JF001238.

Seats, K.J., Lawrence, J.F., Prieto, G.A., 2012. Improved ambient noise correlation functions using Welch's method. Geophysical Journal International 188, 513–523. doi:10.1111/j.1365-246X.2011.05263.x.

Shreve, R.L., 1972. Movement of Water in Glaciers. Journal of Glaciology 11, 205–214. URL: https://www.cambridge.org/core/journals/journal-of-glaciology/article/movement-of-water-in-glaciers/68CF63EE098E16BE0072489E0BBC16CB, doi:10.3189/S002214300002219X.

Stehly, L., Campillo, M., Shapiro, N.M., 2006. A study of the seismic noise from its long-range correlation properties. Journal of Geophysical Research: Solid Earth 111. URL: https://agupubs.onlinelibrary.wiley.com/doi/abs/10.1029/2005JB004237, doi:https://doi.org/10.1029/2005JB004237, arXiv:https://agupubs.onlinelibrary.wiley.com/doi/pdf/10.1029/2005JB004237.

Stevens, N.T., Zoet, L.K., Hansen, D.D., Alley, R.B., Roland, C.J., Schwans, E., Shepherd, C.S., 2024. Icequake insights on transient glacier slip mechanics near channelized subglacial drainage. Earth and Planetary Science Letters 627, 118513. URL: https://www.sciencedirect.com/science/article/pii/S0012821X23005253, doi:10.1016/j.epsl.2023.118513.

Stuart, G., Murray, T., Gamble, N., Hayes, K., Hodson, A., 2003. Characterization of englacial channels by ground-penetrating radar: An example from austre Brøggerbreen, Svalbard. Journal of Geophysical Research: Solid Earth 108. URL: https://onlinelibrary.wiley.com/doi/abs/10.1029/2003JB002435, doi:10.1029/2003JB002435. _eprint: https://onlinelibrary.wiley.com/doi/pdf/10.1029/2003JB002435.

Swiss Seismological Service (SED) At ETH Zurich, 1985. Temporary deployments in switzerland associated with glacier monitoring. https://doi.org/10.12686/SED/NETWORKS/4D. doi:10.12686/SED/NETWORKS/4D. eTH Zurich. Other.

Thyng, K.M., Greene, C.A., Hetland, R.D., Zimmerle, H.M., DiMarco, S.F., 2016. True colors of oceanography: Guidelines for effective and accurate colormap selection. Oceanography 29, 9–13. doi:10.5670/oceanog.2016.66.

Tsai, V.C., Minchew, B., Lamb, M.P., Ampuero, J.P., 2012. A physical model for seismic noise generation from sediment transport in rivers. Geophysical Research Letters 39. doi:https://doi.org/10.1029/2011GL050255.

Walder, J.S., 1986. Hydraulics of Subglacial Cavities. Journal of Glaciology 32, 439–445. URL: https://www.cambridge.org/core/journals/journal-of-glaciology/article/hydraulics-of-subglacial-cavities/BCE3C58A3BE0D07880FBD66D694F1BAD, doi:10.3189/S0022143000012156.

Walder, J.S., Fowler, A., 1994. Channelized subglacial drainage over a deformable bed. Journal of Glaciology 40, 3–15. doi:10.3189/S0022143000003750.

Walter, F., Gräff, D., Lindner, F., Paitz, P., Köpfli, M., Chmiel, M., Fichtner, A., 2020. Distributed acoustic sensing of microseismic sources and wave propagation in glaciated terrain. Nature Communications 11, 2436. URL: https://www.nature.com/articles/s41467-020-15824-6, doi:10.1038/s41467-020-15824-6. number: 1 Publisher: Nature Publishing Group.

Wapenaar, K., 2006. Green's function retrieval by cross-correlation in case of one-sided illumination. Geophysical Research Letters 33. URL: https://onlinelibrary.wiley.com/doi/abs/10.1029/2006GL027747, doi:10.1029/2006GL027747. _eprint: https://onlinelibrary.wiley.com/doi/pdf/10.1029/2006GL027747.

Weertman, J., 1972. General theory of water flow at the base of a glacier or ice sheet. Reviews of Geophysics 10, 287–333. doi:10.1029/RG010i001p00287. publisher: John Wiley & Sons, Ltd.

Werder, M., Alexandre, L., Funk, M., 2009. Dye tracing a jökulhlaup: I. Subglacial water transit speed and water-storage mechanism. Journal of Glaciology 55, 889–898. doi:10.3189/002214309790152447.

Werder, M.A., Hewitt, I.J., Schoof, C.G., Flowers, G.E., 2013. Modeling channelized and distributed subglacial drainage in two dimensions. Journal of Geophysical Research: Earth Surface 118, 2140–2158. URL: https://agupubs.onlinelibrary.wiley.com/doi/abs/10.1002/jgrf.20146, doi:https://doi.org/10.1002/jgrf.20146, arXiv:https://agupubs.onlinelibrary.wiley.com/doi/pdf/10.1002/jgrf.20146.